An isogeometric formulation of the Koiter's theory for buckling and initial post-buckling analysis of composite shells

Leonardo Leonetti[a,*], Domenico Magisano[a], Francesco Liguori[a], Giovanni Garcea[a]

[a]*Dipartimento di Ingegneria Informatica, Modellistica, Elettronica e Sistemistica Università della Calabria 87036 Rende (Cosenza), Italy*

Abstract

Numerical formulations of the Koiter theory allow the efficient prediction, through a reduced model, of the behavior of shell structures when failure is dominated by buckling. In this work, we propose an isogeometric version of the method based on a solid-shell model. A NURBS interpolation is employed on the middle surface of the shell to accurately describe the geometry and the high continuity typical of the displacement field in buckling problems and to directly link the CAD model to the structural one. A linear interpolation is then adopted through the thickness together with a modified generalized constitutive matrix, which allows us to easily eliminate thickness locking and model multi-layered composites. Reduced integration schemes, which take into account the continuity of the shape functions, are used to avoid interpolation locking and make the integration faster. A Mixed Integration Point strategy makes it possible to transform the displacement model into a mixed (stress-displacement) one, required by the Koiter method to obtain accurate predictions, without introducing stress interpolation functions. The result is an efficient numerical tool for buckling and initial post-buckling analysis of composite shells, characterized by a low number of DOFs and integration points and by a simple and quick construction of the reduced model.

Keywords: Geometric nonlinearities, isogeometric analysis, composite shells, reduced integration, MIP

1. Introduction

Composite shells are nowadays employed as primary structural elements in a very wide range of applications. Their success is mainly due to the high strength/weight ratio that is crucial for lightweight structures. The failure of such elements often occurs because of buckling phenomena which make them sensitive to material, geometrical and load imperfections [1, 2]. Thousands of equilibrium path evaluations can be required in order to detect the worst imperfection case in terms of failure load. Once discretization techniques are applied to the continuum problem, the arc-length nonlinear analysis is the standard approach for reconstructing the equilibrium path of such structures. This analysis consists in solving step-by-step a system of nonlinear equations where the unknowns are the discrete degrees of freedom (DOFs) and the load factor. Although this method easily provides the desired information for assigned data, it is too time consuming [3] and inappropriate for an imperfection sensitivity analysis with current CPUs when fine meshes are needed. Furthermore, the stacking sequence has proven to strongly affect the buckling and post-buckling response of the shells [4–6] and the design of an optimal layup can significantly increase the load-carrying capability [7]. Consequently, the need for an optimization process leads to a further computational burden and requires more efficient tools of analysis and design.

For these reasons, a great amount of research has focused on developing reduced order models (ROMs) based on the finite element (FE) implementation [8–20] of the Koiter theory of elastic stability [21]. This

*Corresponding author

Email addresses: leonardo.leonetti@unical.it (Leonardo Leonetti), domenico.magisano@unical.it (Domenico Magisano), francesco.liguori@unical.it (Francesco Liguori), giovanni.garcea@unical.it (Giovanni Garcea)

numerical strategy, known as Koiter method and initially proposed in [22–24], is capable of furnishing, with an acceptable computational cost, an accurate prediction [1] of the limit load value and the initial post-critical behavior for a very large number of imperfections. From this perspective it seems to be more effective in the design stage of slender structures.

The ROM consists in approximating the unknown fields using the initial path tangent and restricted number m of buckling modes associated to the first buckling loads and the corresponding quadratic correctives. In this way, the response of the structure is defined by a reduced system of nonlinear equations where the unknowns are the load factor and m modal amplitudes and the coefficients correspond to 2nd, 3rd and 4th order energy variations. The most convenient aspect of the method is that the effects of geometrical imperfections can be included a posteriori in the reduced system of the perfect structure. A very large number of imperfections can be considered in this way, since each of them only requires the solution of the reduced system, with a very low computational cost (usually fractions of seconds).

The global operations, which involve the total number of DOFs, are limited to the construction of the ROM of the perfect structure and are comparable to those required by a linearized buckling analysis. However, optimization processes of geometry and layup strongly modify the structural behavior and require repetition many times. In this case, the total computational cost is highly dependent on the discretization. A solid-shell FE model [25–29] proves to be particularly convenient for the construction of the ROM, since it allows us to avoid the use of finite rotations, typical of other exact [30] or corotational [31] shell models, which make the evaluation of the high order strain energy variations complex and expensive. Although a large number of locking free linear solid-shell elements are available, their behavior is not sufficiently accurate when modeling curved geometry and, as a consequence, a fine discretization is required. On the other hand, increasing the interpolation order drastically reduces the computational convenience of the element because of the high number of DOFs and the time consuming integration and assembly of the quantities [32].

An interesting alternative is given by the isogeometric analysis (IGA) [33, 34] based on NURBS shape functions. In contrast to Lagrangian functions, one of their feature is the possibility of elevating the order of the interpolation with little change in the number of DOFs. The number of integration points required for the numerical integration is also kept quite low because of the high continuity of the shape functions [35, 36]. Other important features are the exact reproduction of the geometry regardless of the mesh adopted and the possibility of a simple link between the CAD model and structural analysis. These aspects make IGA very attractive in particular in buckling problems, where a highly continuous solution is often expected [37, 38] and the accurate representation of the geometry is an important requirement for an accurate analysis [1].

Despite the many advantages, some difficulties have to be overcome. Although the use of very high order shape functions eliminates interpolation lockings, the order elevation increases the computational efforts for the integration and the assembly of the discrete quantities. Also the solution of the discrete problem becomes slower because the stiffness matrix sparsity decreases. For these reasons C_1-quadratic and C_2-cubic NURBS interpolations are often preferred, even though they exhibit locking phenomena. The inter-element high continuity of the interpolation makes it no longer possible to employ element-wise reduced integrations and strategies like Assumed Natural Strain (ANS) [39] effectively; indeed, they only alleviate but do not completely eliminate locking and prove to be an unsuitable choice for very thin shells. This also happens when using mixed formulations with stress shape functions defined at element level.

Conversely, a satisfactory cure for locking is represented by mixed formulations where continuous stress shape functions [40, 41] are assumed. In this case, the total number of DOFs increases with respect to the initial displacement formulation and the static condensation of the stress variables, usually employed in finite element approaches and performed at element level, can only be carried out at patch level leading to a full condensed stiffness matrix. An effective alternative is the use of displacement formulations with patch-wise reduced integration rules [35] which have been shown to alleviate and, in same cases, eliminate lockings in linear elastic problems [36] and at the same time have the additional advantage of reducing the number of integration points. This strategy seems more attractive than the mixed formulation since it preserves the stiffness matrix sparsity without introducing additional unknowns and allows a more efficient integration.

However, it has been shown in [16, 24] that the Koiter method requires a mixed formulation in order to avoid a locking phenomenon in the evaluation of the fourth-order coefficients of the reduced system of equations and to increase the range of validity of the ROM, which gets worse in displacement formulations

when the slenderness of the structure increases [16, 42] and the pre-buckling path exhibits even small nonlinearities. This aspect can also be observed in path-following analyses [16, 43, 44] where displacement formulations lead to a slow convergence rate of the Newton scheme when slender structures are analyzed. This is due to the bad estimate of the stresses when evaluated using extrapolated displacements. In the Koiter analysis this phenomenon is much more evident because the equilibrium path is directly extrapolated using the ROM, and an equilibrium error is not corrected by an iterative scheme, so affecting the accuracy of the method. On the contrary mixed formulations avoid this drawback because the stresses are directly extrapolated. Furthermore, the joint use of a Green-Lagrange strain measure and of a mixed Hellinger-Reissner variational formulation [15, 16], leads to a $3rd$ order polynomial dependence of the strain energy on the discrete DOFs with the consequence of the zeroing of all the fourth order strain energy variations.

In this work, we propose an isogeometric numerical formulation of the Koiter theory for the analysis of composite shells which exploits the advantages of a solid-shell model. A linear through-the-thickness interpolation is considered for geometry and displacements. The nonlinear model is based on a Total-Lagrangian formulation with the use of the Green-Lagrange strain measure. Inspired by the FE approach proposed by Sze [43], the Green-Lagrange strains are linearized along the thickness direction, allowing the definition of a modified generalized constitutive matrix which effectively eliminates thickness locking and leads to accurate predictions for multi-layered composites, without introducing additional through-the-thickness DOFs [45–47]. The displacement field and the geometry are rewritten in terms of semi-sum and semi-difference of the top and bottom surface quantities. The model so obtained is described by middle surface coordinates only, allowing us to interpolate geometry and displacements using bivariate NURBS of generic order and continuity. Each control point is equipped with six DOFs but, in contrast to traditional shell models, only displacement DOFs are employed. Shear and membrane locking, which already occur in linear elastic problems for low order NURBS [48], are even more evident in the nonlinear range. Different patch-wise reduced integration rules [35, 36], previously proposed for linear analysis, are investigated in stability problems with the aim of eliminating interpolation lockings and increasing the computational efficiency when C_1-quadratic and C_2-cubic NURBS are adopted.

To obtain the mixed description of the problem, required by the Koiter formulation, the Mixed Integration Point (MIP) strategy, recently proposed in [44, 49] for finite element path-following analyses, is here extended to the proposed isogeometric Koiter analysis. It consists in relaxing the constitutive equations at each integration point, making it possible to rewrite the strain energy of the model in a pseudo Hellinger-Reissner form. We will demonstrate that this approach pushes the efficiency of the Koiter analysis to the limit and, at the same time, preserves the accuracy of the ROM without the need for stress shape functions and the previously discussed drawback.

The paper is organized as follows: section 2 presents the isogeometric solid-shell model for composite shell structures; in section 3 we discuss the buckling and initial post-buckling analysis based on the Koiter method focusing on the patch-wise reduced integration and reformulation of the analysis based on MIP strategy; numerical tests to validate the proposed isogeometric formulation of the Koiter theory for the analysis of common composite structural elements are presented in section 4; finally the conclusions are discussed in section 5.

2. The isogeometric solid-shell model

An isogeometric solid-shell model for Koiter analysis of composite shells is derived in this section. Geometry and displacement fields expressed in terms of quantities on the middle surface of the shell are interpolated with NURBS function of generic order. The model, based on Total Lagrangian formulation and Green-Lagrange strain measure, is then derived. It extends the FE model proposed in [43].

2.1. NURBS basics

A B-Spline curve is represented as

$$\mathbf{u}[\xi] = \sum_{i=1}^{n} N_i^p[\xi]\mathbf{P}_i = \mathbf{N}[\xi]\mathbf{P} \tag{1}$$

where $\mathbf{P}_i$, $i = 1 \cdots n$ are control points and $N_i^p(\xi)$ are the set of B-Spline basis functions, which are piecewise polynomial functions of order p. The latter are defined by a set of non-decreasing real numbers $\Xi = [\xi_1, \xi_2, ..., \xi_{n+p+1}]$ known as knot vectors. More details on the B-Spline parametrization can be found in [50]. B-spline basis functions are calculated recursively by using the formula

$$N_i^p[\xi] = \frac{\xi - \xi_i}{\xi_{i+p} - \xi_i} N_i^{p-1}[\xi] + \frac{\xi_{i+p+1} - \xi}{\xi_{i+p+1} - \xi_{i+1}} N_{i+1}^{p-1}[\xi]$$

for $p \geq 1$ and starting from piecewise constant functions ($p = 0$) defined as

$$N_i^0[\xi] = \begin{cases} 1, & \text{if} \quad \xi_i \leq \xi < \xi_{i+1} \\ 0, & \text{otherwise.} \end{cases}$$

The regularity of B-Spline basis functions is given by $r = p - s$ where p and s are the order used for the basis functions and the multiplicity of the knot ξ_i respectively. NURBS extend the B-spline concept in order to represent circular arcs and conic sections exactly. NURBS are obtained by a projective transformation of B-splines extending Eq.(1) by using

$$R_i^p[\xi] = \frac{N_i^p[\xi] w_i}{\sum_i^n N_i^p[\xi] w_i} \tag{2}$$

as shape functions. It is worth noting that all properties of B-Splines are maintained and, in particular, B-Spline basis is retrieved when all the weights are equal.

By applying the tensor product, the NURBS surface is constructed in a similar way to Eq.(1) as

$$\mathbf{u}[\xi, \eta] = \sum_{i=1}^{n} \sum_{j=1}^{m} R_i^p[\xi] M_j^q[\eta] \mathbf{P}_{ij} = \mathbf{N}[\xi, \eta] \mathbf{P} \tag{3}$$

where $\Xi = [\xi_1, \xi_2 ... \xi_{n+p+1}]$ and $\mathcal{H} = [\eta_1, \eta_2 ... \eta_{m+q+1}]$ are two knot vectors, R_i^p and M_j^q are the one-dimensional basis functions over these knot vectors and $\mathbf{P}_{ij}$ defines a set of $n \times m$ control points. The tensor product of the knot vectors Ξ and $\mathcal{H}$ defines a mesh of quadrilateral "isogeometric elements".

Weights, as well as control points of the initial geometry, are provided by the CAD model while suitable algorithms exist for the refinement required to approximate the unknown solution [33, 50]. The geometry is always represented exactly regardless of the mesh adopted.

2.2. Shell kinematics

Convective curvilinear shell coordinates $\boldsymbol{\xi} = [\xi, \eta, \zeta]$ with (ξ, η) representing middle surface coordinates and ζ being the shell thickness coordinate are employed in this Total Lagrangian formulation. The position of material points in the current configuration is given in terms of their position vector $\mathbf{X}(\xi, \eta, \zeta)$ in the reference configuration and the displacement state $\mathbf{d}(\xi, \eta, \zeta)$, cf Fig. 1

$$\mathbf{x}(\xi, \eta, \zeta) = \mathbf{X}(\xi, \eta, \zeta) + \mathbf{d}(\xi, \eta, \zeta). \tag{4}$$

The covariant basis vectors in the undeformed and deformed configuration are obtained from the corresponding partial derivatives of the position vectors $\mathbf{X}$ and $\mathbf{x}$, respectively

$$\mathbf{G}_i = \mathbf{X}_{,i}\,, \qquad \mathbf{g}_i = \mathbf{x}_{,i} = \mathbf{G}_i + \mathbf{d}_{,i} \qquad \text{with} \;\; i = 1, 2, 3\,, \tag{5}$$

where $()_{,i}$ denotes the partial derivative with respect to ith components of $\boldsymbol{\xi}$. The contravariant basis vectors follow from the dual basis condition: $\mathbf{g}_i \cdot \mathbf{g}^j = \mathbf{G}_i \cdot \mathbf{G}^j = \delta_i^j$ and the metric coefficients are $g_{ij} = \boldsymbol{g}_i \cdot \boldsymbol{g}_j$ and $G_{ij} = \mathbf{G}_i \cdot \mathbf{G}_j$ with $(i, j = 1, 2, 3)$. The motion of material points from the initial reference configuration to the current configuration is described by the deformation map $\mathbf{F} : \mathbf{x} \rightarrow \mathbf{X}$

$$\mathbf{F} = \frac{\partial \mathbf{x}}{\partial \mathbf{X}} = \mathbf{g}_i \otimes \mathbf{G}^i \tag{6}$$

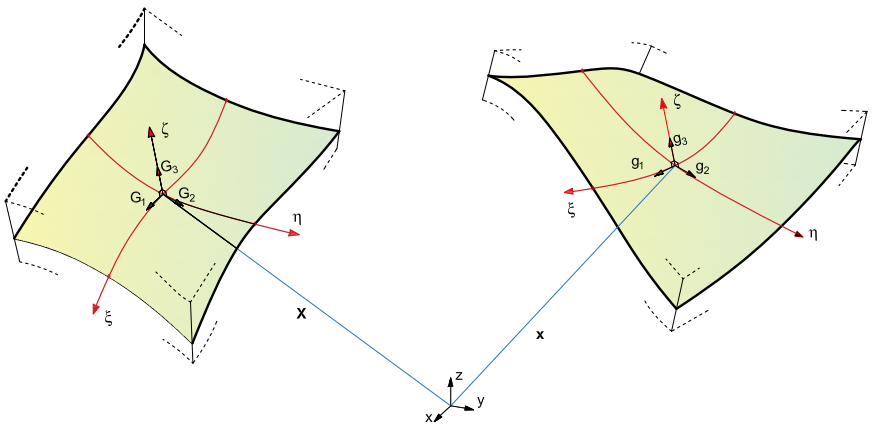


Figure 1: Undeformed and deformed shell geometry.

and the Einstein convention of summing on repeated indexes is adopted from now on.

Using the deformation gradient in Eq.(6) and the metric tensor coefficients g_{ij} and G_{ij}, the Green-Lagrange strain tensor can be expressed as

$$\mathbf{E} = \frac{1}{2}\left(\mathbf{F}^T\,\mathbf{F} - \mathbf{I}\right) = \bar{E}_{ij}\,\mathbf{G}^i \otimes \mathbf{G}^j \tag{7}$$

with

$$\bar{E}_{ij} = \frac{1}{2}\left(\mathbf{X}_{,i}\cdot\mathbf{d}_{,j} + \mathbf{d}_{,i}\cdot\mathbf{X}_{,j} + \mathbf{d}_{,i}\cdot\mathbf{d}_{,j}\right) \quad \text{with} \quad i,j = 1,2,3 \tag{8}$$

where $(\cdot)$ means scalar product.

Assuming a linear through-the-thickness interpolation the position vector is expressed as

$$\mathbf{X} = \mathbf{X}_0[\xi,\eta] + \zeta\mathbf{X}_n[\xi,\eta] \tag{9}$$

where

$$\mathbf{X}_0 = \frac{1}{2}\left(\mathbf{X}[\xi,\eta,1] + \mathbf{X}[\xi,\eta,-1]\right), \quad \mathbf{X}_n = \frac{1}{2}\left(\mathbf{X}[\xi,\eta,1] - \mathbf{X}[\xi,\eta,-1]\right)$$

with $\zeta = 1$ and $\zeta = -1$ identifying the top and the bottom surface of the shell respectively.

Similarly, the displacement field $\mathbf{d} = \mathbf{d}_0[\xi,\eta] + \zeta\mathbf{d}_n[\xi,\eta]$ is described as a combination of the displacements

$$\mathbf{d}_0 = \frac{1}{2}\left(\mathbf{d}[\xi,\eta,1] + \mathbf{d}[\xi,\eta,-1]\right), \quad \mathbf{d}_n = \frac{1}{2}\left(\mathbf{d}[\xi,\eta,1] - \mathbf{d}[\xi,\eta,-1]\right).$$

The same convective coordinates $\boldsymbol{\xi}$ are used for expressing the interpolation of the discrete model.

2.3. The isogeometric solid-shell element

The numerical model is obtained interpolating the geometry and the displacement field using the shape functions in Eq.(3)

$$\mathbf{X}[\boldsymbol{\xi}] = \mathbf{N}_d[\boldsymbol{\xi}]\mathbf{X}_e, \quad \mathbf{d}[\boldsymbol{\xi}] = \mathbf{N}_d[\boldsymbol{\xi}]\mathbf{d}_e \tag{10}$$

where $\mathbf{d}_e = [\mathbf{d}_{0e}, \mathbf{d}_{ne}]$ and $\mathbf{X}_e = [\mathbf{X}_{0e}, \mathbf{X}_{ne}]$ collect the element control points for displacement and geometry. The matrix $\mathbf{N}_d[\boldsymbol{\xi}]$ collects the interpolation functions

$$\mathbf{N}_d[\boldsymbol{\xi}] \equiv \left[\mathbf{N}[\xi,\eta], \zeta\mathbf{N}[\xi,\eta]\right] \tag{11}$$

where $\zeta \in [-1,+1]$ and $\mathbf{N}[\xi,\eta]$ are bivariate NURBS (3), functions of the middle surface coordinates only.

Adopting a Voigt notation, the Green-Lagrange covariant strain components in Eq.(8) are collected in vector $\bar{\mathbf{E}} = [\bar{E}_{\xi\xi}, \bar{E}_{\eta\eta}, 2\bar{E}_{\xi\eta}, \bar{E}_{\zeta\zeta}, 2\bar{E}_{\eta\zeta}, 2\bar{E}_{\xi\zeta}]^T$, that, exploiting Eq.(10), becomes

$$\bar{\mathbf{E}} = \left(\boldsymbol{\mathcal{L}}[\boldsymbol{\xi}] + \frac{1}{2}\boldsymbol{\mathcal{Q}}[\boldsymbol{\xi}, \mathbf{d}_e] \right) \mathbf{d}_e, \tag{12}$$

where $\boldsymbol{\mathcal{L}}[\boldsymbol{\xi}] \equiv \boldsymbol{\mathcal{Q}}[\boldsymbol{\xi}, \mathbf{X}_e]$ and $\boldsymbol{\mathcal{Q}}$ is so defined

$$\boldsymbol{\mathcal{Q}}[\boldsymbol{\xi}, \mathbf{d}_e] \equiv \begin{bmatrix} \mathbf{d}_e^T \mathbf{N}_{d,\xi}^T \mathbf{N}_{d,\xi} \\ \mathbf{d}_e^T \mathbf{N}_{d,\eta}^T \mathbf{N}_{d,\eta} \\ \mathbf{d}_e^T (\mathbf{N}_{d,\xi}^T \mathbf{N}_{d,\eta} + \mathbf{N}_{d,\eta}^T \mathbf{N}_{d,\xi}) \\ \mathbf{d}_e^T \mathbf{N}_{d,\zeta}^T \mathbf{N}_{d,\zeta} \\ \mathbf{d}_e^T (\mathbf{N}_{d,\zeta}^T \mathbf{N}_{d,\eta} + \mathbf{N}_{d,\eta}^T \mathbf{N}_{d,\zeta}) \\ \mathbf{d}_e^T (\mathbf{N}_{d,\xi}^T \mathbf{N}_{d,\zeta} + \mathbf{N}_{d,\zeta}^T \mathbf{N}_{d,\xi}) \end{bmatrix}. \tag{13}$$

By truncation, the linearized covariant strains

$$\bar{\mathbf{E}} \approx \begin{bmatrix} \bar{\mathbf{e}}[\xi, \eta] + \zeta\, \bar{\boldsymbol{\chi}}[\xi, \eta] \\ \bar{E}_{\zeta\zeta}[\xi, \eta] \\ \bar{\boldsymbol{\gamma}}[\xi, \eta] \end{bmatrix} \tag{14}$$

where

$$\bar{\mathbf{e}}[\xi, \eta] \equiv \begin{bmatrix} \bar{E}_{\xi\xi}[\xi, \eta, 0] \\ \bar{E}_{\eta\eta}[\xi, \eta, 0] \\ 2\bar{E}_{\xi\eta}[\xi, \eta, 0] \end{bmatrix} \quad \bar{\boldsymbol{\chi}}[\xi, \eta] \equiv \begin{bmatrix} \bar{E}_{\xi\xi,\zeta}[\xi, \eta, 0] \\ \bar{E}_{\eta\eta,\zeta}[\xi, \eta, 0] \\ 2\bar{E}_{\xi\eta,\zeta}[\xi, \eta, 0] \end{bmatrix} \quad \bar{\boldsymbol{\gamma}}[\xi, \eta] \equiv \begin{bmatrix} 2\bar{E}_{\eta\zeta}[\xi, \eta, 0] \\ 2\bar{E}_{\xi\zeta}[\xi, \eta, 0] \end{bmatrix}$$

are collected in the vector of generalized covariant strains $\bar{\boldsymbol{\varepsilon}}[\xi, \eta] \equiv \left[\bar{\mathbf{e}}, \bar{E}_{\zeta\zeta}, \bar{\boldsymbol{\chi}}, \bar{\boldsymbol{\gamma}}\right]^T$. In order to simplify the notation, the dependence of the quantities on ξ, η will be omitted from now on, when clear.

The generalized stress components, once the kinematic model is assumed, are automatically given by assuring the invariance of the internal work. By collecting the contravariant stress components $\bar{\mathbf{S}} \equiv [\bar{S}_{\xi\xi}, \bar{S}_{\eta\eta}, \bar{S}_{\xi\eta}, \bar{S}_{\zeta\zeta}, \bar{S}_{\eta\zeta}, \bar{S}_{\xi\zeta}]^T$, the work conjugate variables with $\bar{\boldsymbol{\varepsilon}}$ are obtained by

$$\begin{aligned} \mathcal{W} &= \int_V \bar{\mathbf{S}}^T \bar{\mathbf{E}} dV = \int_\Omega \left(\bar{\boldsymbol{\mathcal{N}}}^T \bar{\mathbf{e}} + \bar{\boldsymbol{\mathcal{M}}}^T \bar{\boldsymbol{\chi}} + \bar{s}_{\zeta\zeta} \bar{E}_{\zeta\zeta} + \bar{\boldsymbol{\mathcal{T}}}^T \bar{\boldsymbol{\gamma}} \right) \\ &= \int_\Omega \bar{\boldsymbol{\sigma}}^T \bar{\boldsymbol{\varepsilon}} d\Omega \end{aligned} \tag{15}$$

where, from now on, $\int_\Omega (...)\, \Omega = 2 \int_{\xi_i}^{\xi_{i+1}} \int_{\eta_i}^{\eta_{i+1}} (...)\, det(\mathbf{J}[\xi, \eta, 0]) d\xi d\eta$ and $\mathbf{J}$ denotes the Jacobian matrix $\mathbf{J}[\xi, \eta, \zeta] = [\mathbf{G}_1,\ \mathbf{G}_2,\ \mathbf{G}_3]^T$.

The generalized contravariant stresses $\bar{\boldsymbol{\sigma}} \equiv \left[\bar{\boldsymbol{\mathcal{N}}}, \bar{s}_{\zeta\zeta}, \bar{\boldsymbol{\mathcal{M}}}, \bar{\boldsymbol{\mathcal{T}}}\right]^T$ in Eq.(15) are then

$$\begin{aligned} \bar{\boldsymbol{\mathcal{N}}} &\equiv \frac{1}{2} \int_{-1}^{1} \bar{\boldsymbol{\sigma}}_p d\zeta \quad \bar{\boldsymbol{\mathcal{M}}} \equiv \frac{1}{2} \int_{-1}^{1} \zeta \bar{\boldsymbol{\sigma}}_p d\zeta \\ \bar{s}_{\zeta\zeta} &\equiv \frac{1}{2} \int_{-1}^{1} \bar{S}_{\zeta\zeta} d\zeta \quad \bar{\boldsymbol{\mathcal{T}}} \equiv \frac{1}{2} \int_{-1}^{1} \bar{\boldsymbol{\tau}} d\zeta \end{aligned} \tag{16}$$

with

$$\bar{\boldsymbol{\sigma}}_p = \begin{bmatrix} \bar{S}_{\xi\xi} \\ \bar{S}_{\eta\eta} \\ \bar{S}_{\xi\eta} \end{bmatrix} \quad \bar{\boldsymbol{\tau}} = \begin{bmatrix} \bar{S}_{\xi\zeta} \\ \bar{S}_{\eta\zeta} \end{bmatrix}.$$

2.4. The mapping to the physical domain

The relation between the contravariant stresses and covariant strains in tensor notation and the corresponding Cartesian ones is

$$\mathbf{E} = \mathbf{J}^{-1}\bar{\mathbf{E}}\mathbf{J}^{-T} \quad \text{and} \quad \mathbf{S} = \mathbf{J}^{T}\bar{\mathbf{S}}\mathbf{J}, \tag{17}$$

that in Voigt notation can be written as

$$\mathbf{E} = \mathbf{T}_E\bar{\mathbf{E}} \quad \text{and} \quad \mathbf{S} = \mathbf{T}_S\bar{\mathbf{S}} \tag{18}$$

with $\mathbf{T}_S = \mathbf{T}_E^{-T}$.

From Eq.(9) $\mathbf{J} = \mathbf{J}_0[\xi,\eta] + \zeta\mathbf{J}_n[\xi,\eta]$ and its inverse can be linearized with respect to ζ as

$$\mathbf{J}^{-1}[\xi,\eta] = \mathbf{J}_0^{-1}[\xi,\eta] + \zeta\mathbf{J}_n^{-1}[\xi,\eta] \tag{19}$$

where it is possible to obtain $\mathbf{J}_n^{-1}$ by satisfying up to the first order in ζ the equation $\mathbf{J}\mathbf{J}^{-1} = \mathbf{I}$, that implies

$$\mathbf{J}_n^{-1} = \mathbf{J}_0^{-1}\mathbf{J}_n\mathbf{J}_0^{-1}.$$

Substituting Eq.(19) in Eq.(18) and maintaining only the linear terms in ζ we obtain the linearized expression of $\mathbf{T}_E = \mathbf{T}_{E0} + \zeta\mathbf{T}_{En}$. In particular letting

$$\mathbf{T}_{E0} = \begin{bmatrix} \mathbf{T}^0_{ee} & \mathbf{T}^0_{e\zeta} & \mathbf{T}^0_{e\gamma} \\ \mathbf{T}^0_{\zeta e} & T^0_{\zeta\zeta} & \mathbf{T}^0_{\zeta\gamma} \\ \mathbf{T}^0_{\gamma e} & \mathbf{T}^0_{\gamma\zeta} & \mathbf{T}^0_{\gamma\gamma} \end{bmatrix}, \qquad \mathbf{T}_{En} = \begin{bmatrix} \mathbf{T}^n_{ee} & \mathbf{T}^n_{e\zeta} & \mathbf{T}^n_{e\gamma} \\ \mathbf{T}^n_{\zeta e} & T^n_{\zeta\zeta} & \mathbf{T}^n_{\zeta\gamma} \\ \mathbf{T}^n_{\gamma e} & \mathbf{T}^n_{\gamma\zeta} & \mathbf{T}^n_{\gamma\gamma} \end{bmatrix}$$

and maintaining the linear terms in ζ only, we have

$$\mathbf{E} = \mathbf{T}_E\bar{\mathbf{E}} = \begin{bmatrix} \mathbf{e} + \zeta\boldsymbol{\chi} \\ E_{\zeta\zeta} \\ \boldsymbol{\gamma} \end{bmatrix}. \tag{20}$$

Eq. (20) can be expressed in terms of the generalized strains as

$$\boldsymbol{\varepsilon} = \mathbf{T}_\epsilon\bar{\boldsymbol{\varepsilon}} \tag{21}$$

where $\boldsymbol{\varepsilon} = [\mathbf{e}, E_{\zeta\zeta}, \boldsymbol{\chi}, \boldsymbol{\gamma}]$ and

$$\mathbf{T}_\epsilon = \begin{bmatrix} \mathbf{T}^0_{ee} & \mathbf{T}^0_{e\zeta} & \mathbf{0}_{3\times3} & \mathbf{T}^0_{e\gamma} \\ \mathbf{T}^0_{\zeta e} & T^0_{\zeta\zeta} & \mathbf{0}_{1\times3} & \mathbf{T}^0_{\zeta\gamma} \\ \mathbf{T}^n_{ee} & \mathbf{T}^n_{e\zeta} & \mathbf{T}^0_{ee} & \mathbf{T}^n_{e\gamma} \\ \mathbf{T}^0_{\gamma e} & \mathbf{T}^0_{\gamma\zeta} & \mathbf{0}_{2\times3} & \mathbf{T}^0_{\gamma\gamma} \end{bmatrix}.$$

Combining Eqs.(12), (14) and (21) it is possible to obtain the Cartesian generalized strain-displacement relationship

$$\boldsymbol{\varepsilon} = \left(\mathbf{L}_e + \frac{1}{2}\mathbf{Q}_e[\mathbf{d}_e]\right)\mathbf{d}_e \tag{22}$$

where

$$\mathbf{Q}_e[\mathbf{u}]\mathbf{v} = \mathbf{Q}_e[\mathbf{v}]\mathbf{u} \qquad \forall\mathbf{u},\mathbf{v}. \tag{23}$$

2.5. Modified generalized constitutive matrix

The homogenization technique proposed in [15, 43] is employed. A modified generalized constitutive matrix $\mathbf{C}_\epsilon$ is derived by integrating the constitutive law of each lamina and assuming a constant with ζ stress $S_{\zeta\zeta}$ through the layers in order to eliminate thickness locking. In this way an accurate prediction of the global behavior in terms of stresses and displacements is obtained.

The thickness locking free generalized constitutive law in the global reference system is

$$\boldsymbol{\sigma}[\xi,\eta] = \mathbf{C}_\epsilon\boldsymbol{\varepsilon}[\xi,\eta]. \tag{24}$$

3. Koiter IGA based on mixed integration points

When comparing FE formulations of the Koiter theory based on a purely displacement-based formulation and a mixed one, it has been shown in many works (see for example [15, 16]) that the latter provides a superior performance. In particular, the use of stress and displacement DOFs as independent variables leads to a more efficient construction of the ROM and makes it accurate for a wider range. The improved accuracy is much more evident when the slenderness of the structure gets higher and the pre-critical path presents some nonlinearities. In [51, 52] it has been shown how the stress interpolation produces locking-free solutions only when the shape functions are continuous over the patch of elements. In this way, the total number of unknowns significantly increases due to the extra stress variables, which cannot be condensed at element level as is usual in the FEM context and it is not convenient. In this work we use an isogeometric version of the Koiter method. Some conflicting aspects are evident. A mixed formulation would lead to an accurate Koiter analysis free from locking, but would compromise the overall efficiency because of the extra stress variables. On the other hand, the displacement formulation is plagued by locking and decreases the range of validity of the ROM. Recently, in [35, 36] patch-wise reduced integrations were successfully proposed for eliminating locking in linear analyses with displacement NURBS interpolations. The main idea of this work is to investigate the use of patch-wise reduced integrations to handle interpolation locking in constructing the ROM using the displacement solid-shell model derived in the previous section. The stresses at the integration points are then chosen as independent variables inspired by the mixed integration point (MIP) strategy proposed in [44] for path-following finite element analyses and adopted in IGA in [49, 53]. In this way the accuracy and efficiency of the ROM is preserved avoiding the use of a stress interpolation.

The standard Koiter approach, described in detail in[1, 15], is now briefly recalled and the steps of the algorithms are particularized to IGA using the MIP strategy and the patch-wise integration.

3.1. The nonlinear model and the numerical integration

We consider a slender hyperelastic structure subject to conservative loads $p[\lambda]$ proportionally increasing with the amplifier factor λ. The equilibrium is expressed by the virtual work equation

$$\Phi[u]'\,\delta u - \lambda \hat{p}\,\delta u = 0 \quad , \quad u \in \mathcal{U}\ ,\ \delta u \in \mathcal{T} \tag{25}$$

where $u \in \mathcal{U}$ is the field of configuration variables, $\Phi[u]$ denotes the strain energy, $\mathcal{T}$ is the tangent space of $\mathcal{U}$ at u and a prime is used to express the Frechèt derivative with respect to u. We assume that $\mathcal{U}$ will be a linear manifold so that its tangent space $\mathcal{T}$ will be independent of u. When a mixed format is adopted the configuration variables u collect both displacement and stress fields.

The displacement based IGA formulation previously presented allows us to express the strain energy of the element as a sum of element contributions $\Phi[u] \equiv \sum_e \Phi_e[\mathbf{d}_e]$

$$\Phi_e[\mathbf{d}_e] \equiv \int_{\Omega_e} \left(\frac{1}{2} \boldsymbol{\varepsilon}^T \mathbf{C}_\epsilon \boldsymbol{\varepsilon} \right) d\Omega_e \tag{26}$$

where Ω_e is the element domain and a numerical integration is usually adopted.

3.1.1. Locking and patch-wise reduced integrations

Note that the same NURBS interpolation is employed over the middle surface of the shell for all the displacement components. As is well known, this produces interpolation locking when low order interpolations are considered. The linear term in Eq.(22) can be plagued by standard shear and membrane locking, which then occurs even in small deformation problems. Furthermore, when a Total Lagrangian formulation is used to describe the nonlinear behavior a more evident additional locking occurs as consequence of the different approximation of the linear and the quadratic Green-Lagrange strain contributions in Eq.(22).

Recently, patch-wise integration rules, which take into account the inter-element high continuity of the displacement interpolation have been proposed [35, 36] and applied to linear elastic problems. In our opinion, these works represent an important development in IGA. The d-dimensional target space, that is the space

for the integration of the strain energy (as well as the stiffness matrix), of order p and regularity r, labeled as $\mathcal{S}_r^p$, is exactly integrated by a number of $\approx ((p-r)/2)^d$ integration points per element, distributed over the patch, significantly lower than in standard Gauss quadrature rules. For the full integration, due to the product of the shape functions and their derivatives, p is twice the order of the splines and r is the continuity order minus one. This means that, for example, for C_1-quadratic and C_2-cubic splines the full integration spaces are $\mathcal{S}_0^4$ and $\mathcal{S}_1^6$ respectively.
Positions and weights of the integration points are not equal for each element, but are evaluated, once and for all, in a pre-processing phase and depend on r, p and patch mesh. The algorithms which provide these kinds of integration rules can be found in [35, 36] and are very efficient. Their computational burden is just a small fraction of the total cost of a linear analysis and negligible compared to a nonlinear analysis. We refer to [35, 36] for all the details.

The patch-wise exact integration of a given space $\mathcal{S}_r^p$ also opens up new possibilities for patch-wise reduced integration schemes. In fact p and r can be selected by the user and are not required to be those for the exact integration of the problem space. If the integration space presents spurious modes, more points than the minimum number strictly required by the space are utilized in order to remove them. In this case the approximation space is said to be over-integrated and labeled as $\bar{\mathcal{S}}_r^p$. The number of additional integration points is proportional to the number of boundary elements and, then, becomes negligible when the mesh gets finer. Again, we refer to [35, 36] for the details. With respect to the element-wise reduced integrations, an appropriate selection of the patch-wise reduced integration rules makes it possible to avoid spurious modes, alleviate or eliminate interpolation locking in the linear elastic range and further reduce the number of integration points.

Being that in patch-wise rules the number of integration points n can be different element-by-element, the strain energy can then be evaluated as

$$\Phi_e[\mathbf{d}_e] \equiv \frac{1}{2}\sum_{g=1}^{n} \boldsymbol{\varepsilon}_g[\mathbf{d}_e]^T \mathbf{C}_g \boldsymbol{\varepsilon}_g[\mathbf{d}_e]\, w_g \tag{27}$$

where subscript g denotes quantities evaluated at the integration point $[\xi_g, \eta_g]$, w_g is the product of the corresponding weight and the determinant of the Jacobian matrix $\mathbf{J}$ evaluated at the integration point and $\mathbf{C}_g$ is $\mathbf{C}_\epsilon$ at the integration point.

The use of a displacement-based IGA model is then theoretically very accurate and efficient and represents, potentially, a reliable choice from the point of view of the discrete approximation and the efficiency of the integration with respect to standard FE interpolation of the same order if interpolation locking is avoided.

3.2. The mixed integration point strategy

In Koiter analysis, regardless of the quality of the discrete approximation, a mixed format in stress and displacement is required to achieve accuracy and efficiency.

The fundamental idea of the mixed integration point (MIP) strategy is to relax the constitutive equations at the level of each integration point. This is made by rewriting the strain energy in a pseudo Hellinger-Reissner form on the element

$$\Phi_e[\mathbf{u}_e] \equiv \sum_{g=1}^{n} \left(\boldsymbol{\sigma}_g^T \boldsymbol{\varepsilon}_g[\mathbf{d}_e] - \frac{1}{2}\boldsymbol{\sigma}_g^T \mathbf{C}_g^{-1} \boldsymbol{\sigma}_g \right) w_g \tag{28}$$

where the stresses at each integration point $\boldsymbol{\sigma}_g$ are now independent variables being

$$\mathbf{u}_e = \begin{bmatrix} \boldsymbol{\sigma}_1 \\ \vdots \\ \boldsymbol{\sigma}_n \\ \mathbf{d}_e \end{bmatrix} \tag{29}$$

From the stationary condition with respect to $\boldsymbol{\sigma}_g$ we obtain the constitutive law at the integration point g

$$\mathbf{s}_{g\sigma} \equiv \boldsymbol{\varepsilon}_g[\mathbf{d}_e] - \mathbf{C}_g^{-1}\boldsymbol{\sigma}_g \tag{30}$$

that, if substituted in Eq.(28), again furnishes the displacement formulation in Eq.(27). This means that we only change the format, from displacement to mixed, not the discrete approximation of the problem and the true equilibrium path obtained with the two formulations, when a path-following scheme is adopted, is exactly the same as the initial displacement formulation [44].

Another important consequence of the MIP rewriting of the problem equations is that, when a Green-Lagrange strain measure is used as in the present Total Lagrangian solid-shell model, the polynomial dependence of the strain energy on the discrete parameters $\mathbf{u}_e$ in the MIP format is of the 3rd order only, instead of the 4th order of the initial displacement formulation.

3.3. The implementation of the Koiter method using mixed integration points

The asymptotic approach is based on a third order Taylor expansion of Eq.(25), in terms of load factor λ and modal amplitudes α_i. We refer readers to [1, 15] for recent developments of the method and more detail.

Letting $u_i \in \mathcal{T}$ be a generic variation of the displacement field and denoting with a bold symbol the discrete FEM counterpart of the continuum quantities, and referring to the solid-shell finite element model presented in [15], the construction of the reduced model of the *perfect structure* consists of the following steps.

1. The fundamental path is evaluated as

$$\mathbf{u}^f[\lambda] = \mathbf{u}_0 + \lambda\hat{\mathbf{u}} \;\;,\;\; \mathbf{K}_0\,\hat{\mathbf{u}} = \mathbf{f} \;\;,\;\; \mathbf{K}_0 \equiv \mathbf{K}[\mathbf{u}_0] \tag{31a}$$

   where $\mathbf{K}_0$ and $\mathbf{f}$ are obtained from the following energy equivalence

$$\mathbf{u}_1^T\mathbf{K}_0\mathbf{u}_2 := \Phi_0'' u_1 u_2 \qquad \mathbf{u}_1^T\mathbf{f} = p\; u_1.$$

   and requires the solution of a linear system to evaluate the initial path tangent $\hat{\mathbf{u}}$. A subscript will denote, from now on, the point in which the quantities are evaluated, i.e. $\Phi_0'' \equiv \Phi''[u_0]$ and so on.
2. The buckling modes and loads are obtained from the linearized critical condition consisting of the eigenvalue problem

$$\mathbf{K}[\lambda]\dot{\mathbf{v}} \equiv (\mathbf{K}_0 + \lambda\mathbf{K}_1[\hat{\mathbf{u}}])\dot{\mathbf{v}} = \mathbf{0} \tag{31b}$$

   where $\mathbf{K}_1$ is obtained from the following energy equivalence

$$\mathbf{u}_1^T\mathbf{K}_1\mathbf{u}_2 = \Phi_0'''\hat{u}u_1u_2.$$

3. The $(m \times (m+1))/2 + 1$ quadratic corrective FE vectors $\mathbf{w}_{ij}, \hat{\hat{\mathbf{w}}}$ are obtained by the solution of the linear systems

$$\begin{aligned} &\mathbf{K}_b\hat{\hat{\mathbf{w}}} + \hat{\hat{\mathbf{f}}} + \sum_{k=1}^{m} c_k\hat{\mathbf{f}}_k = \mathbf{0} \qquad \text{with} \quad c_k = \dot{\mathbf{v}}_k^T\hat{\hat{\mathbf{f}}} \\ &\mathbf{K}_b\mathbf{w}_{ij} + \mathbf{f}_{ij} + \sum_{k=1}^{m} c_k\hat{\mathbf{f}}_k = \mathbf{0} \quad \text{with} \quad c_k = \dot{\mathbf{v}}_k^T\mathbf{f}_{ij} \end{aligned} \tag{31c}$$

   in which $\mathbf{K}_b \equiv \mathbf{K}_0 + \lambda_b\mathbf{K}_1$, $\hat{\mathbf{f}}_k = \mathbf{K}_1\dot{\mathbf{v}}_k$, λ_b is a reference value of the bifurcation cluster, usually the first buckling load and $\mathbf{f}_{ij}, \mathbf{f}_{00}$ are defined as a function of modes $\dot{\mathbf{v}}_i$ and $\hat{\mathbf{u}}$ by the energy equivalences

$$\delta\mathbf{w}^T\mathbf{f}_{ij} = \Phi'''\dot{v}_j\dot{v}_j\delta w$$
$$\delta\mathbf{w}^T\hat{\hat{\mathbf{f}}} = \Phi'''\hat{u}^2\delta w$$

4. The construction of the reduced system of equations

$$\begin{aligned} r_k[\lambda,\alpha_i] \equiv \mu_k[\lambda] + (\lambda_k-\lambda)\alpha_k - \frac{1}{2}\lambda^2\sum_{i=1}^{m}\alpha_i\mathcal{C}_{ik} + \frac{1}{2}\sum_{i,j=1}^{m}\alpha_i\alpha_j\mathcal{A}_{ijk} \\ + \frac{1}{6}\sum_{i,j,h=1}^{m}\alpha_i\alpha_j\alpha_h\mathcal{B}_{ijhk} = 0, \quad k = 1\cdots m \end{aligned} \tag{31d}$$

is carried out by evaluating the energy terms for $i,j,h,k = 1\cdots m$ as sum of element contributions

$$\begin{aligned} \mathcal{A}_{ijk} =& \Phi'''\dot{v}_i\dot{v}_j\dot{v}_k \\ \mathcal{C}_{ik} =& \Phi''_b\hat{\hat{w}}w_{ik} \\ \mathcal{B}_{ijhk} =& -\Phi''_b(w_{ij}w_{hk}+w_{ih}w_{jk}+w_{ik}w_{jh}) \\ \mu_k[\lambda] =& \frac{1}{2}\lambda^2\Phi'''\hat{u}^2\dot{v}_k \end{aligned}$$

where

$$\Phi''_b u_1 u_2 = (\Phi''_0 + \lambda_b\Phi'''\hat{u})u_1u_2 \quad \forall u_1,u_2.$$

The evaluation of the equilibrium path, to be repeated for each additional imperfection, is obtained by solving the modified reduced system

$$r_k[\lambda,\alpha_i] + \tilde{\mu}_k[\lambda,\alpha_i] = 0$$

where $\tilde{\mu}_k$ represents the effect of the imperfection, and can be evaluated as in [1].

3.4. Strain energy variations using Mixed Integration Points

In the following $\mathbf{u}_{ig} = \{\boldsymbol{\sigma}_{ig}, \mathbf{d}_{ie}\}$ will denote the vector representation on the integration point g of u_i.

The first variation of (28) is

$$\Phi'_e u_1 = \sum_{g=1}^{n}\begin{bmatrix}\boldsymbol{\sigma}_{1g}\\ \mathbf{d}_{1e}\end{bmatrix}^T\begin{bmatrix}\mathbf{s}_{g\sigma}\\ \mathbf{s}_{gd}\end{bmatrix}w_g \tag{32a}$$

with

$$\begin{cases}\mathbf{s}_{g\sigma} \equiv \boldsymbol{\varepsilon}_g[\mathbf{d}_e] - \mathbf{C}_g^{-1}\boldsymbol{\sigma}_g \\ \mathbf{s}_{gd} \equiv \mathbf{B}_g[\mathbf{d}_e]^T\boldsymbol{\sigma}_g.\end{cases} \tag{32b}$$

and $\mathbf{B}_g[\mathbf{d}_e] = \mathbf{L}_g + \mathbf{Q}_g[\mathbf{d}_e]$.

The second variation of (28) is

$$\Phi''_e u_1 u_2 = \sum_{g=1}^{n}\left\{\boldsymbol{\sigma}_{1g}^T\mathbf{B}_g[\mathbf{d}_e]\mathbf{d}_{2e} + \boldsymbol{\sigma}_{2g}^T\mathbf{B}_g[\mathbf{d}_e]\mathbf{d}_{1e} + \boldsymbol{\sigma}_g^T\mathbf{Q}_g[\mathbf{d}_{1e}]\mathbf{d}_{2e}\right\}w_g. \tag{32c}$$

Letting

$$\varepsilon^Q_{gk} = \mathbf{d}_{1e}^T\boldsymbol{\Psi}_{gk}\mathbf{d}_{2e}.$$

the kth component of vector $\mathbf{Q}_g[\mathbf{d}_{1e}]\mathbf{d}_{2e}$ the following expression holds

$$\boldsymbol{\sigma}_g^T\mathbf{Q}_g[\mathbf{d}_{1e}]\mathbf{d}_{2e} \equiv \sum_k \sigma_{gk}\,\varepsilon^Q_{gk} = \mathbf{d}_{1e}^T\boldsymbol{\mathcal{G}}[\boldsymbol{\sigma}_g]\mathbf{d}_{2e}$$

with

$$\boldsymbol{\mathcal{G}}[\boldsymbol{\sigma}_g] = \sum_k \sigma_{gk}\boldsymbol{\Psi}_{gk}. \tag{32d}$$

In matrix form the second variation of (28) then becomes

$$\begin{aligned}\Phi''_e u_1 u_2 &= \sum_{g=1}^{n} \begin{bmatrix}\boldsymbol{\sigma}_{1g}\\ \mathbf{d}_{1e}\end{bmatrix}^T \begin{bmatrix}-\mathbf{C}_g^{-1} & \mathbf{B}_g\\ \mathbf{B}_g^T & \boldsymbol{\mathcal{G}}_g\end{bmatrix} \begin{bmatrix}\boldsymbol{\sigma}_{2g}\\ \mathbf{d}_{2e}\end{bmatrix} w_g \\ &= \sum_g \mathbf{u}_{1g}^T \mathbf{K}_g \mathbf{u}_{2g}\end{aligned} \tag{32e}$$

where $\boldsymbol{\mathcal{G}}_g \equiv \boldsymbol{\mathcal{G}}_e[\boldsymbol{\sigma}_g]$.

The second variation can also be written in vector form introducing the *incremental force vector* so defined

$$\Phi''_e u_1 u_2 = \sum_g \mathbf{u}_{1g}^T \mathbf{s}'_g[\mathbf{u}_{2g}] \quad \text{with} \quad \mathbf{s}'_g[\mathbf{u}_{2g}] \equiv \begin{bmatrix}-\mathbf{C}_g^{-1}\boldsymbol{\sigma}_{2g} + \mathbf{B}_g \mathbf{d}_{2e}\\ \mathbf{B}_g^T \boldsymbol{\sigma}_{2g} + \boldsymbol{\mathcal{G}}_g \mathbf{d}_{2e}\end{bmatrix} \tag{32f}$$

The third variation of the strain energy is

$$\Phi''_e u_1 u_2 u_3 = \sum_{g=1}^{n} \left\{ \boldsymbol{\sigma}_{1g}^T \mathbf{Q}_g[\mathbf{d}_{3e}]\mathbf{d}_{2e} + \boldsymbol{\sigma}_{2g}^T \mathbf{Q}_g[\mathbf{d}_{3e}]\mathbf{d}_{1e} + \boldsymbol{\sigma}_{3g}^T \mathbf{Q}_g[\mathbf{d}_{1e}]\mathbf{d}_{2e} \right\} w_g \tag{32g}$$

that can also be written in vector form introducing the *secondary force vector* as

$$\Phi'''_e \delta u_1 \delta u_2 \delta u_3 = \sum_g \mathbf{u}_{1g}^T \mathbf{s}''_g[\mathbf{u}_{2g}, \mathbf{u}_{3g}] \quad \text{with} \quad \mathbf{s}''_g[\mathbf{u}_{2g}, \mathbf{u}_{3g}] \equiv \begin{bmatrix}\mathbf{Q}_g[\mathbf{d}_{3e}]\mathbf{d}_{2e}\\ \mathbf{Q}_g[\mathbf{d}_{3e}]^T \boldsymbol{\sigma}_{2g} + \boldsymbol{\mathcal{G}}_g[\boldsymbol{\sigma}_{3g}]\mathbf{d}_{2e}\end{bmatrix} \tag{32h}$$

Note that all fourth order strain energy variations of the initial displacement based formulation are identically zero due to the 3rd order polynomial dependence of the strain energy on the discrete parameters.

Finally, as usual, for each element vector $\mathbf{y}_e$ and matrix $\mathbf{Y}_e$ the global quantities are obtained using standard assemblage operations as

$$\mathbf{y} = \sum_e \boldsymbol{\mathcal{A}}_e^T \mathbf{y}_e, \quad \mathbf{Y} = \sum_e \boldsymbol{\mathcal{A}}_e^T \mathbf{Y}_e \boldsymbol{\mathcal{A}}_e. \tag{33}$$

while scalar quantities are simply sums of element contributions.

3.5. Solution of the Koiter linear systems and eigenvalue problem in condensed form

Koiter analysis requires the evaluation of a series of linear systems and an eigenvalue problem. Their solution can be obtained by static condensation of the stress variables. This is an important aspect of the proposed IGA MIP formulation which allows us to eliminate them at integration point level, maintaining the computational cost of the displacement one.

3.5.1. Fundamental path

Eq.(31a) at the element level becomes

$$\begin{bmatrix}-\mathbf{C}_1^{-1} w_1 & & & \mathbf{L}_1 w_1\\ & \ddots & & \vdots\\ & & -\mathbf{C}_n^{-1} w_n & \mathbf{L}_n w_n\\ \mathbf{L}_1^T w_1 & \dots & \mathbf{L}_n^T w_n & \mathbf{0}\end{bmatrix} \begin{bmatrix}\hat{\boldsymbol{\sigma}}_1\\ \vdots\\ \hat{\boldsymbol{\sigma}}_n\\ \hat{\mathbf{d}}_e\end{bmatrix} = \begin{bmatrix}\mathbf{0}\\ \vdots\\ \mathbf{0}\\ \mathbf{f}_e\end{bmatrix} \tag{34}$$

By performing a static condensation of the stress correction $\dot{\boldsymbol{\sigma}}_g$, locally defined at the integration point, we obtain

$$\hat{\boldsymbol{\sigma}}_g = \mathbf{C}_g \mathbf{L}_g \hat{\mathbf{d}}_e \tag{35}$$

and then

$$\mathbf{K}_{0e}^c \hat{\mathbf{d}}_e = \mathbf{f}_e \quad \text{with} \quad \mathbf{K}_{0e}^c = \sum_{g=1}^{n} \left(\mathbf{L}_g^T \mathbf{C}_g \mathbf{L}_g \right) w_g \tag{36}$$

where the condensed element tangent stiffness matrix $\mathbf{K}_{0e}^c$ coincides with the classical displacement-based one

3.5.2. Buckling problem

The buckling problem can be written as

$$\begin{bmatrix} -\mathbf{C}_1^{-1}w_1 & & & (\mathbf{L}_1+\lambda\mathbf{Q}_1[\hat{\mathbf{d}}_e])w_1 \\ & \ddots & & \vdots \\ & & -\mathbf{C}_n^{-1}w_n & (\mathbf{L}_n+\lambda\mathbf{Q}_n[\hat{\mathbf{d}}_e])w_n \\ (\mathbf{L}_1+\lambda\mathbf{Q}_1[\hat{\mathbf{d}}_e])^T w_1 & \dots & (\mathbf{L}_n+\lambda\mathbf{Q}_n[\hat{\mathbf{d}}_e])^T w_n & \lambda\sum_g \boldsymbol{\mathcal{G}}_g[\hat{\boldsymbol{\sigma}}_g]w_g \end{bmatrix} \begin{bmatrix} \dot{\boldsymbol{\sigma}}_1 \\ \vdots \\ \dot{\boldsymbol{\sigma}}_n \\ \dot{\mathbf{d}}_e \end{bmatrix} = \begin{bmatrix} \mathbf{0} \\ \vdots \\ \mathbf{0} \\ \mathbf{0} \end{bmatrix} \tag{37}$$

and also in this case, eliminating the stresses of the integration points

$$\dot{\boldsymbol{\sigma}}_g = \mathbf{C}_g(\mathbf{L}_g+\lambda\mathbf{Q}_g[\hat{\mathbf{d}}_e])\dot{\mathbf{d}}_e$$

and substituting in Eq.(37)

$$\left\{\sum_g \left((\mathbf{L}_g+\lambda\mathbf{Q}_g)^T\mathbf{C}_g(\mathbf{L}_g+\lambda\mathbf{Q}_g)+\lambda\boldsymbol{\mathcal{G}}_g[\hat{\boldsymbol{\sigma}}_g]\right)w_g\right\}\dot{\mathbf{d}}_e = \mathbf{0},$$

we obtain the element contribution to the quadratic eigenvalue problem

$$\sum_g (\mathbf{K}^c_{0g}+\lambda\mathbf{K}^c_{1g}+\lambda^2\mathbf{K}^c_{2g})\dot{\mathbf{d}}_e = \mathbf{0}.$$

A linearized problem can also be obtained when the quadratic part of the strain along the fundamental path $\mathbf{Q}_g[\dot{\mathbf{d}}_e]$ is negligible and then

$$\left\{\sum_g \left(\mathbf{L}_g^T\mathbf{C}_g\mathbf{L}_g+\lambda\boldsymbol{\mathcal{G}}_g[\hat{\boldsymbol{\sigma}}_g]\right)w_g\right\}\dot{\mathbf{d}}_e = \mathbf{0}.$$

3.5.3. Quadratic correctives

Finally the linear system in Eq.(31c), letting $c_k = 0$ to simplify the writing, becomes

$$\begin{bmatrix} -\mathbf{C}_1^{-1}w_1 & & & \mathbf{B}_1w_1 \\ & \ddots & & \vdots \\ & & -\mathbf{C}_n^{-1}w_n & \mathbf{B}_nw_n \\ \mathbf{B}_1^Tw_1 & \dots & \mathbf{B}_n^Tw_n & \sum_g \boldsymbol{\mathcal{G}}_g w_g \end{bmatrix}_b \begin{bmatrix} \hat{\dot{\boldsymbol{\sigma}}}_1 \\ \vdots \\ \hat{\dot{\boldsymbol{\sigma}}}_n \\ \hat{\dot{\mathbf{d}}}_e \end{bmatrix} = - \begin{bmatrix} \mathbf{Q}_1[\hat{\mathbf{d}}_e]\dot{\mathbf{d}}_e \\ \vdots \\ \mathbf{Q}_n[\hat{\mathbf{d}}_e]\dot{\mathbf{d}}_e \\ \sum_g \left(\mathbf{Q}_g[\hat{\mathbf{d}}_e]^T\hat{\boldsymbol{\sigma}}_g+\boldsymbol{\mathcal{G}}_g[\hat{\boldsymbol{\sigma}}_g]\dot{\mathbf{d}}_e\right) \end{bmatrix} \tag{38}$$

where subscript b on matrices denotes that they are evaluated in $\mathbf{u}_{bg} = \lambda_b\{\hat{\boldsymbol{\sigma}}_g, \hat{\mathbf{d}}_e\}$.

By condensing out the stress correction at the integration points

$$\hat{\dot{\boldsymbol{\sigma}}}_g = \mathbf{C}_g\mathbf{B}_g\hat{\dot{\mathbf{d}}}_e + \mathbf{C}_g\mathbf{Q}_g[\hat{\mathbf{d}}_e]\dot{\mathbf{d}}_e \tag{39}$$

we obtain the linear system in the condensed form

$$\mathbf{K}_{be}\hat{\dot{\mathbf{d}}}_e = -\hat{\dot{\mathbf{s}}}_c \tag{40}$$

with

$$\begin{aligned} \mathbf{K}_e[\hat{\mathbf{u}}_e] &= \sum_g \left(\mathbf{B}_g^T\mathbf{C}_g\mathbf{B}_g+\boldsymbol{\mathcal{G}}_g[\boldsymbol{\sigma}_g]\right)_b w_g \\ \mathbf{s}_{ce}[\hat{\mathbf{u}}_e] &= \sum_g \left(\mathbf{Q}_g[\hat{\mathbf{d}}_e]^T\hat{\boldsymbol{\sigma}}_g+\boldsymbol{\mathcal{G}}_g[\hat{\boldsymbol{\sigma}}_g]\hat{\mathbf{d}}_e+\mathbf{B}_g^T\mathbf{C}_g\mathbf{Q}_g[\hat{\mathbf{d}}_e]\hat{\mathbf{d}}_e\right)w_g \end{aligned} \tag{41}$$

as the condensed tangent stiffness matrix, that has the same expression as the classical displacement based one but directly depends on the stresses, and the condensed secondary forces respectively.

E_{11}	$E_{22} = E_{33}$	$\nu_{12} = \nu_{13}$	ν_{23}	$G_{12} = G_{13}$	G_{23}
181e9	10.27e9	0.28	0	7.17e9	5.135e9

Table 1: Composite square plate: material properties.

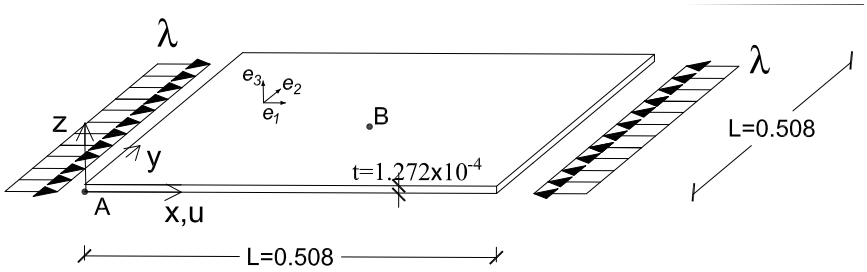


Figure 2: Composite square plate: geometry, load and boundary conditions.

4. Numerical results

The proposed numerical tool is now tested in common composite structures, such as plates, panels and cylinders. The first goal is to test the accuracy of the isogeometric solid-shell model in representing the buckling and post-buckling configuration. To this end, different meshes and numerical integrations are considered for C_1-quadratic and C_2-cubic NURBS interpolations of the displacement field over the middle surface of the shell. The second goal is to assess the accuracy of the ROM built with the proposed MIP isogeometric formulation of the Koiter method by comparing the results with reference solutions obtained by path-following analyses [49] based on the full model.

4.1. Composite square plate under compression

The first test, depicted in Fig.2, is a simply supported laminated plate under compression. The material properties are reported in Table 1. The layup adopted is $[0°/90°]_{4S}$. The test has been studied in [19] using shell elements and in [6] by a Ritz method. Firstly, the accuracy of the proposed isogeometric solid-shell model is tested in the evaluation of the four lowest buckling loads, which are reported in Table 2 and Table 3 for the C_1 and the C_2 interpolation respectively. The corresponding buckling modes are pictured in Fig.3. Different integration schemes are considered as well as the local ANS proposed in [39]. In particular, Table 2 shows the good performance of $\bar{S}_0^2$, which turns out to be the best integration among those considered in terms of both accuracy and efficiency, providing good results for the 8×8 mesh and requiring just ≈ 1 integration point per element. Conversely, ANS and the full integration S_0^4, which require 9 and ≈ 4 integration points per element respectively, prove to be inaccurate because of the interpolation locking. It increases with the slenderness of the plate and slowly vanishes when the mesh is refined. Moreover, Table 3 shows the advantages of a higher continuity in buckling problems, showing that the C_2 interpolation with $\bar{S}_1^3$ and, in particular, S_1^4 integration provides good results even using a 4×4 mesh. $\bar{S}_1^3$ requires ≈ 1 integration point per element but is slightly penalized for coarse meshes by the over-integration, while S_1^4 furnishes exact results for a 8×8 mesh and makes use of ≈ 2.25 integration points per element. The full integration S_1^6, making use of ≈ 6.25 integration points per element, is unusable due to locking phenomena that also hold for the finest mesh.

The equilibrium path in the pre-critical and initial post-critical range is reconstructed using the Koiter method and reported in Fig.4 for C_1 and Fig.5 for C_2. A small geometrical imperfection $\tilde{e}$ with the shape of the first buckling mode and $\|\tilde{e}\|_\infty = 0.01t$ is considered. In addition, a reference solution obtained using a very fine mesh and the standard Riks method, which solves step-by-step the nonlinear equations of the full discrete model, is reported. For this test, just one buckling mode is used in the ROM of the Koiter method which, then, requires that only one nonlinear equation be solved. Looking at Fig.4 we can note

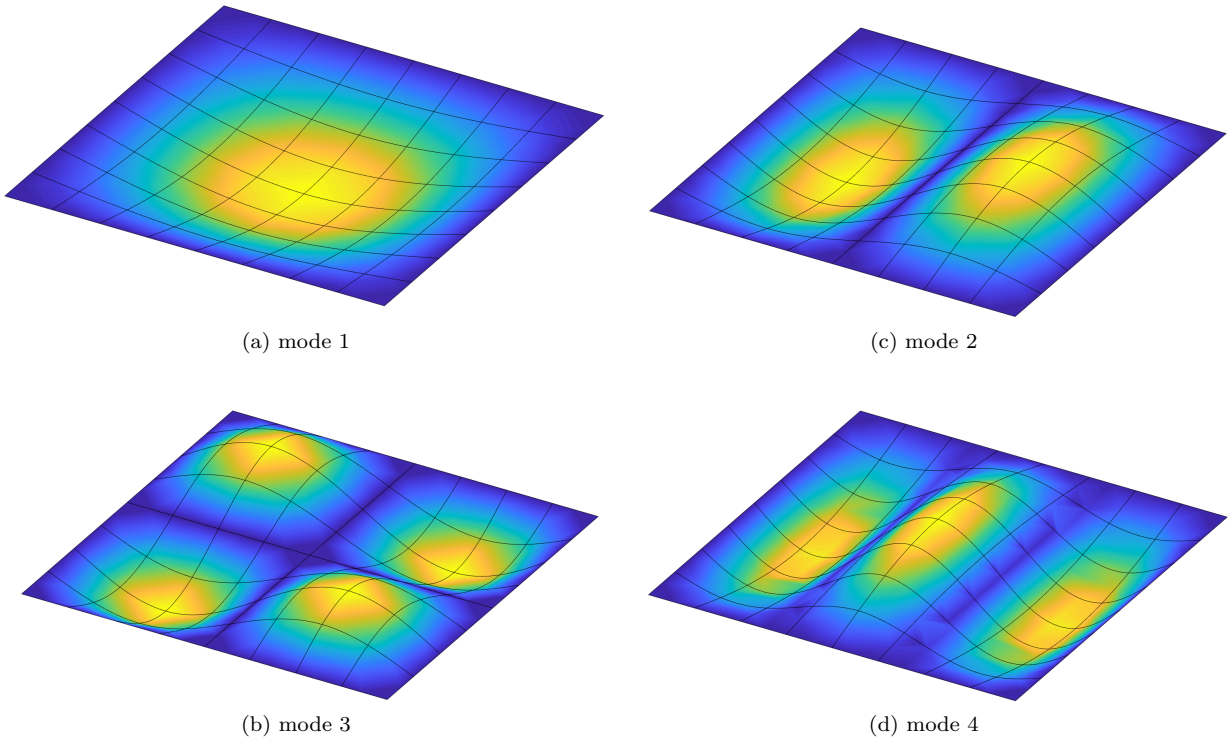
4 elm.				8 elm.				16 elm.			
$\bar{S}_0^2$	S_0^3	S_0^4	ANS	$\bar{S}_0^2$	S_0^3	S_0^4	ANS	$\bar{S}_0^2$	S_0^3	S_0^4	ANS
1.010	1.004	1.185	1.184	1.000	1.002	1.179	1.121	1.000	1.000	1.113	1.006
1.367	$*$	$*$	1.483	1.007	1.073	$*$	1.439	1.000	1.006	1.561	1.064
1.348	$*$	$*$	1.457	1.006	1.071	$*$	1.422	1.000	1.006	1.648	1.076
1.328	$*$	$*$	1.636	1.022	1.015	$*$	1.591	1.000	1.007	$*$	1.188

$* > 2$

Table 2: Composite square plate: first 4 normalized buckling loads for C_1 interpolation.

4 elm.			8 elm.			16 elm.		
$\bar{S}_1^3$	S_1^4	S_1^6	$\bar{S}_1^3$	S_1^4	S_1^6	$\bar{S}_1^3$	S_1^4	S_1^6
1.003	1.000	1.185	1.000	1.000	1.170	1.000	1.000	1.028
1.031	1.030	1.479	1.003	1.000	1.473	1.000	1.000	1.240
1.034	1.028	1.451	1.004	1.000	1.446	1.000	1.000	1.255
1.139	1.012	1.618	1.016	1.002	1.614	1.001	1.000	1.412

Table 3: Composite square plate: first 4 normalized buckling loads for C_2 interpolation.



(a) mode 1 (c) mode 2

(b) mode 3 (d) mode 4

Figure 3: Composite square plate: first 4 buckling modes.

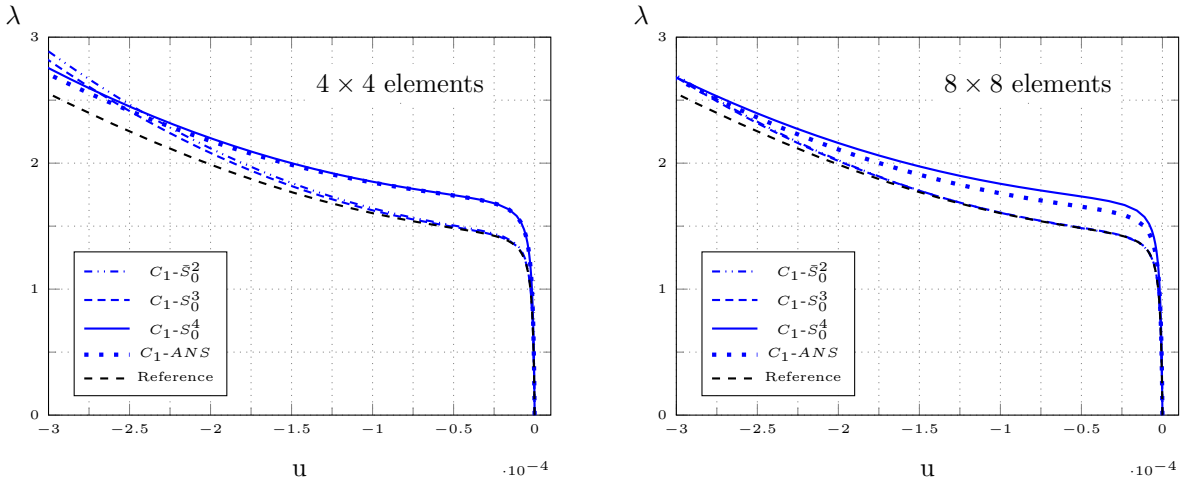


Figure 4: Composite square plate: equilibrium path using the C_1 interpolation

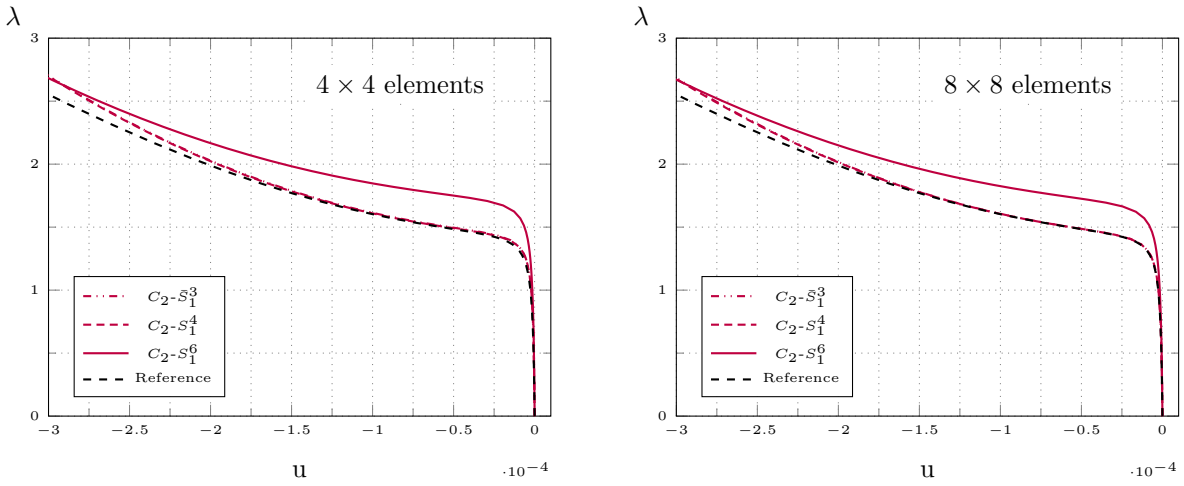


Figure 5: Composite square plate: equilibrium path using the C_2 interpolation

that, although the bifurcation point is almost exact using C_1-$\bar{S}_0^2$, a 4×4 mesh exhibits a stiffer post-buckling response compared to the reference solution as consequence of interpolation locking of the linear and quadratic strains. However, the error becomes much lower by considering a 8×8 mesh. Figure 5, on the other hand, highlights the benefits of a higher continuity: C_2-$\bar{S}_1^3$ and C_2-S_1^4 agree very well with the reference path also for the coarsest mesh.

As a general comment, a drastic reduction in the number of DOFs is achieved with respect to the locking free linear shell elements used in [19] for the same test.

4.2. Composite curved panel under compression

The second test regards a curved panel under compression whose geometry, loads, and boundary conditions are represented in Fig.6. The material properties can be found in Table 4. Two different layups are considered: $[0]_6$ and $[45, -45, 0]_s$. The lamination significantly influences the shape of the buckling modes as illustrated in Fig.7. The slenderness of the panel is much lower than that of the previous test. This means that the effects of the interpolation locking are less evident. This is confirmed by Tables 5, 6, 7 and 8 which show the convergence of the first 4 linearized buckling loads. The high continuity together with the

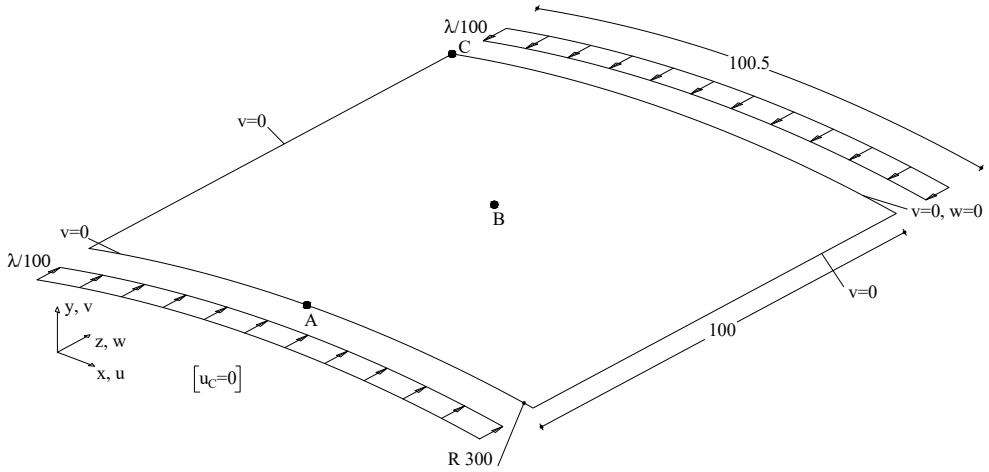


Figure 6: Composite curved panel: geometry and boundary conditions.

E_{11}	$E_{22} = E_{33}$	$\nu_{12} = \nu_{13}$	ν_{23}	$G_{12} = G_{13}$	G_{23}
30.6	8.7	0.29	0.5	3.24	2.9

Table 4: Composite curved panel: material properties.

exact representation of the geometry leads to very good results with all the integration strategies. Again, however, the $\bar{S}_0^2$ for C_1 and S_1^4 and $\bar{S}_1^3$ for C_2 represent the best choices in terms of accuracy and efficiency.

The study of the initial post-buckling behavior of the panel is carried out considering the presence of a geometrical imperfection $\tilde{e}$ that is a combination of the first and the second buckling modes. In particular, it is the difference between them scaled in order to obtain $\|\tilde{e}\|_\infty = 0.1t$. The Koiter solution is evaluated using a ROM based on the first two buckling modes only, since the higher ones are far from the first two, and it is compared with reference paths obtained using a very fine mesh and the standard Riks method for solving the nonlinear equations of the full model. For both the layups, the initial post-buckling exhibits a limit load as shown in Fig.8 and Fig.9 for $[0]_6$ and in Fig.10 and 11 for $[45, -45, 0]_s$. C_1-$\bar{S}_0^2$, C_2-$\bar{S}_1^3$ and C_2-S_1^4 are the best performing strategies, providing a good estimate of the limit loads with a 8×8 mesh, which became practically exact using a 16×16 mesh. Clearly, the Koiter solution differs from the full nonlinear one for very large displacements since the ROM is built for the estimation of the initial post-buckling behavior.

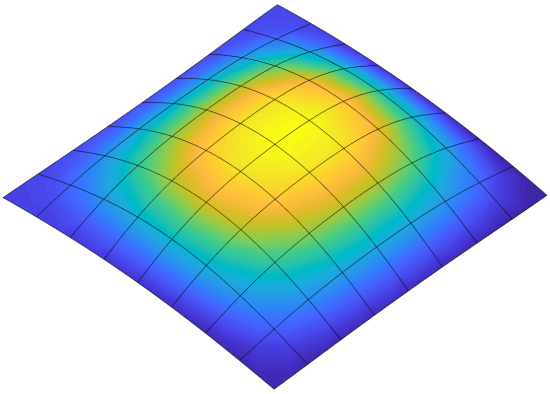
4.3. Laminate composite cylinder subjected to axial compression

The cylinder considered in the following and labelled Z33 was manufactured and tested by DLR (German Aerospace Center) and commonly used as a validation model for numerical developments in the context of laminate composite shell design [1, 54]. The stacking sequence is $_{in}[0/0/19/-19/37/-37/45/-45/51/-$

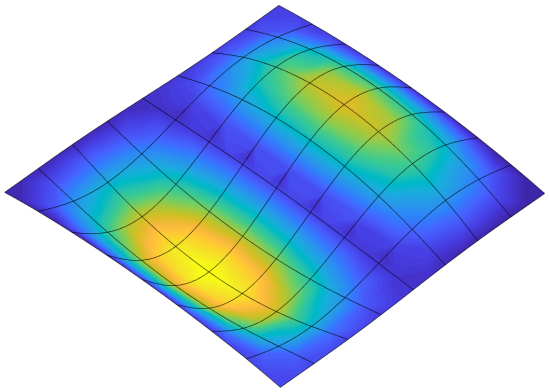
4 elm.				8 elm.				16 elm.			
$\bar{S}_0^2$	S_0^3	S_0^4	ANS	$\bar{S}_0^2$	S_0^3	S_0^4	ANS	$\bar{S}_0^2$	S_0^3	S_0^4	ANS
1.053	1.055	1.078	1.042	1.002	0.998	1.020	1.008	0.995	0.995	0.998	0.996
1.158	1.424	1.694	1.177	1.005	1.008	1.069	1.018	0.996	0.998	1.003	0.997
1.259	1.609	$*$	1.299	1.009	1.035	1.124	1.039	1.003	1.004	1.012	1.003
1.408	1.746	$*$	1.396	1.007	1.061	1.213	1.067	1.003	1.005	1.020	1.004

$*$ > 2

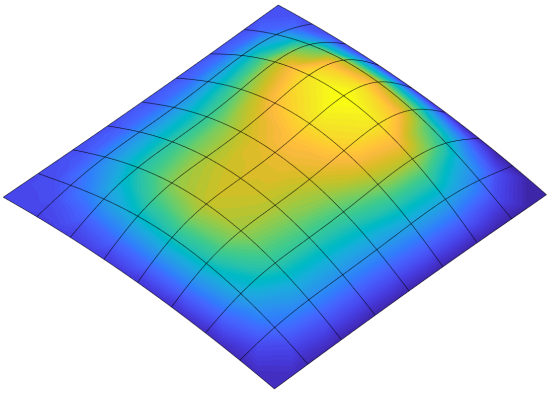
Table 5: Composite curved panel: first 4 normalized buckling loads for $[0]_6$ with C_1 interpolation.



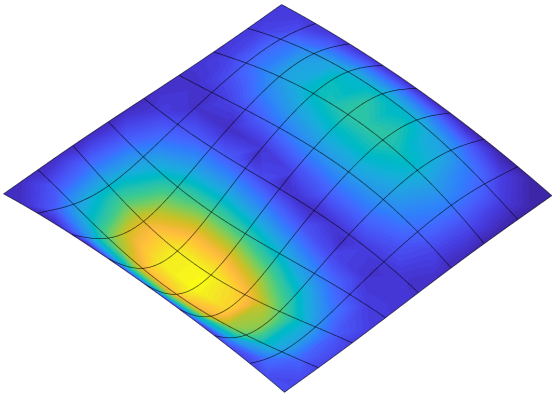
(a) mode 1 $[0]_6$



(c) mode 2 $[0]_6$



(b) mode 1 $[45/-45/0]_s$



(d) mode 2 $[45/-45/0]_s$

Figure 7: Composite curved panel: first and second buckling mode corresponding to two different layups

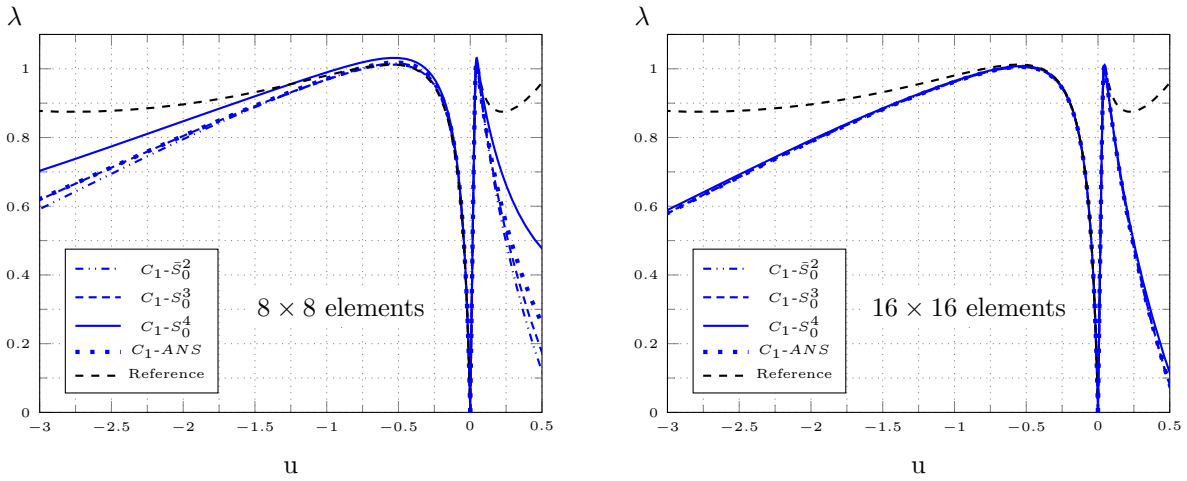


Figure 8: Composite curved panel: equilibrium path for $[0]_6$ and C_1 interpolation

4 elm.				8 elm.				16 elm.			
$\bar{S}_0^2$	S_0^3	S_0^4	ANS	$\bar{S}_0^2$	S_0^3	S_0^4	ANS	$\bar{S}_0^2$	S_0^3	S_0^4	ANS
1.096	1.144	1.263	1.165	1.016	1.018	1.095	1.054	1.001	1.002	1.015	1.004
1.082	1.201	1.656	1.106	1.013	1.010	1.078	1.036	0.998	0.999	1.011	1.001
1.080	1.346	$*$	1.333	1.007	1.010	1.157	1.061	0.998	0.999	1.010	0.999
1.235	1.456	$*$	1.848	1.035	1.073	1.228	1.119	1.003	1.012	1.049	1.011

$* > 2$

Table 6: Composite curved panel: first 4 normalized buckling loads for $[45, -45, 0]_s$ with C_1 interpolation.

4 elm.			8 elm.			16 elm.		
$\bar{S}_1^3$	S_1^4	S_1^6	$\bar{S}_1^3$	S_1^4	S_1^6	$\bar{S}_1^3$	S_1^4	S_1^6
0.995	1.034	1.031	1.001	1.005	1.004	1.001	1.002	1.001
1.000	1.013	1.073	1.001	1.004	1.003	1.001	1.001	1.001
1.008	1.063	1.132	1.003	1.008	1.007	1.002	1.003	1.003
1.014	1.104	1.210	1.004	1.009	1.010	1.002	1.003	1.003

Table 7: Composite curved panel: first 4 normalized buckling loads for $[0]_s$ with C_2 interpolation.

4 elm.			8 elm.			16 elm.		
$\bar{S}_1^3$	S_1^4	S_1^6	$\bar{S}_1^3$	S_1^4	S_1^6	$\bar{S}_1^3$	S_1^4	S_1^6
0.995	1.097	1.110	1.006	1.014	1.018	1.002	1.005	1.004
1.014	1.044	1.068	1.006	1.012	1.015	1.001	1.003	1.003
1.002	1.121	1.167	1.003	1.007	1.014	1.001	1.003	1.002
1.062	1.205	1.280	1.041	1.022	1.061	1.001	1.003	1.003

Table 8: Composite curved panel: first 4 normalized buckling loads $[45, -45, 0]_s$ with C_2 interpolation.

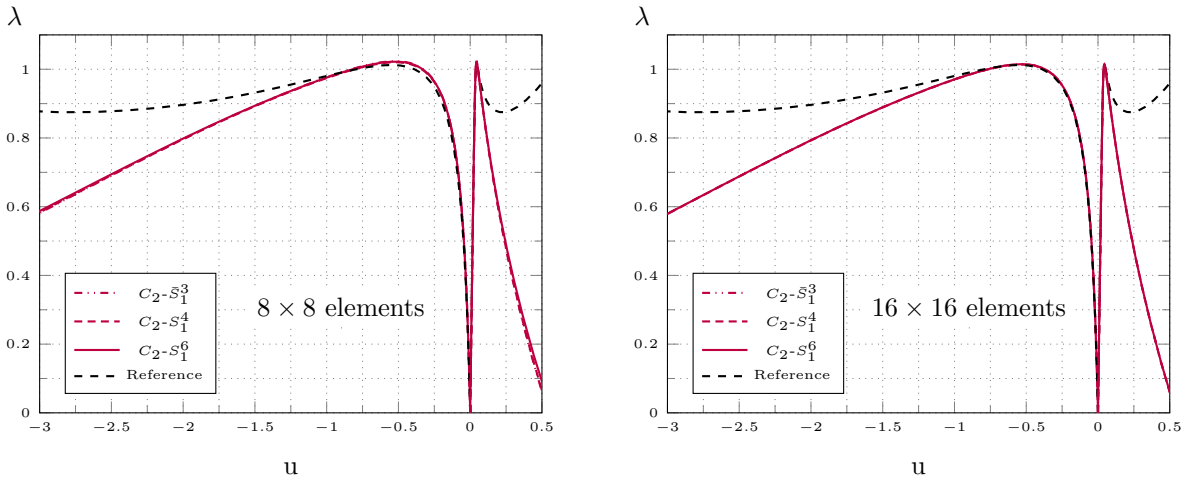


Figure 9: Composite curved panel: equilibrium path for $[0]_6$ and C_2 interpolation

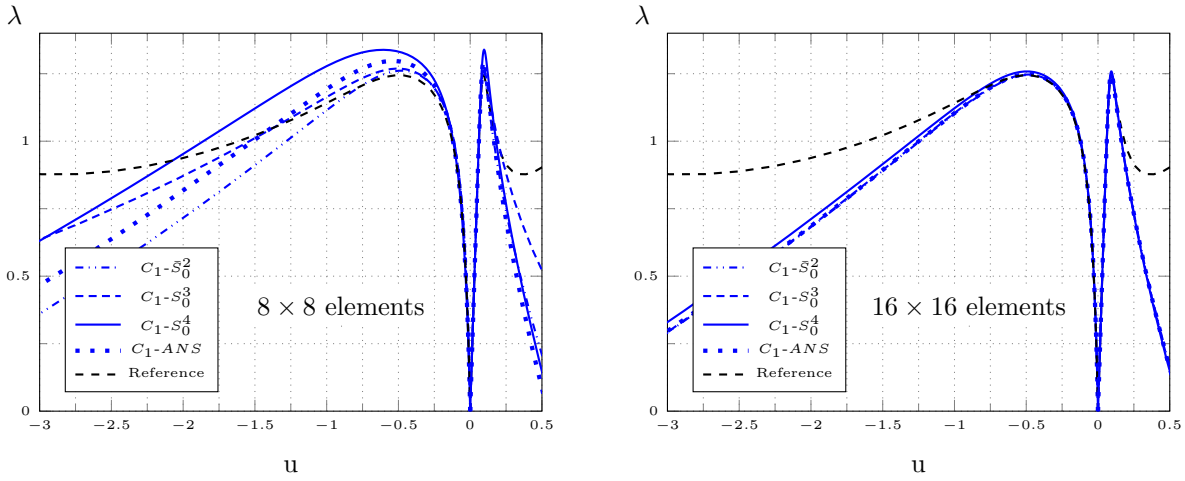


Figure 10: Composite curved panel: equilibrium path for $[45/-45/0]$ and C_1 interpolation

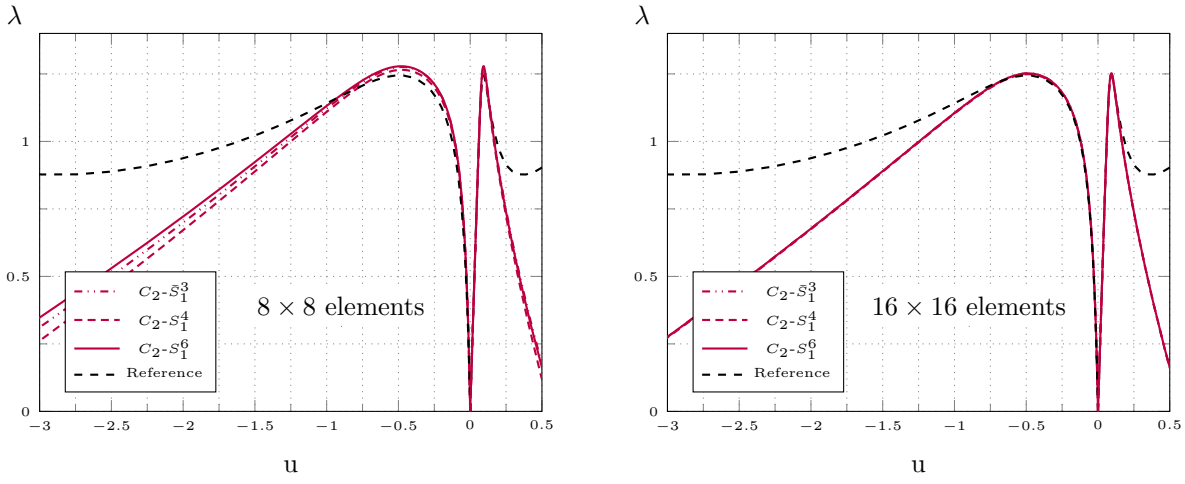


Figure 11: Composite curved panel: equilibrium path for $[45/-45/0]$ and C_2 interpolation

E_{11}	$E_{22} = E_{33}$	ν_{12}	$\nu_{23} = \nu_{13}$	$G_{12} = G_{13} = G_{23}$
123.6	8.7	0.32	0	5.7

Table 9: Laminate composite cylinder: material properties.

12 elm.				24 elm.				48 elm.			
$\bar{S}_0^2$	S_0^3	S_0^4	ANS	$\bar{S}_0^2$	S_0^3	S_0^4	ANS	$\bar{S}_0^2$	S_0^3	S_0^4	ANS
0.957	1.594	$*$	1.658	1.003	1.041	1.200	1.056	1.000	1.002	1.015	1.001
0.960	1.596	$*$	1.664	1.006	1.046	1.200	1.059	1.000	1.002	1.015	1.001
0.959	1.618	$*$	1.661	1.005	1.044	1.200	1.060	1.000	1.002	1.014	1.001
0.962	1.618	$*$	1.719	1.007	1.048	1.208	1.060	1.000	1.002	1.014	1.001

$* > 2$

Table 10: Laminate composite cylinder: first 4 normalized buckling loads with C_1 interpolation.

$51]_{out}$ with the angles measured from the cylinder axis with respect to the outward normal. The cylinder has a height of 510, a radius of $R = 250$ and a wall-thickness of $t = 1.25$, cf Fig.12. The material properties are reported in Table 9

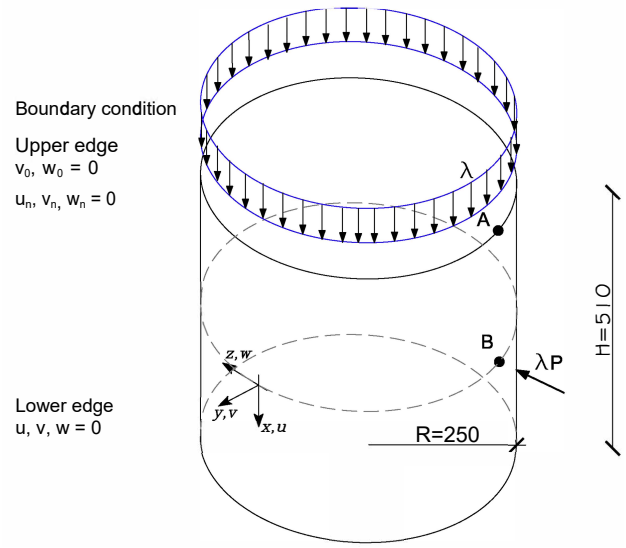


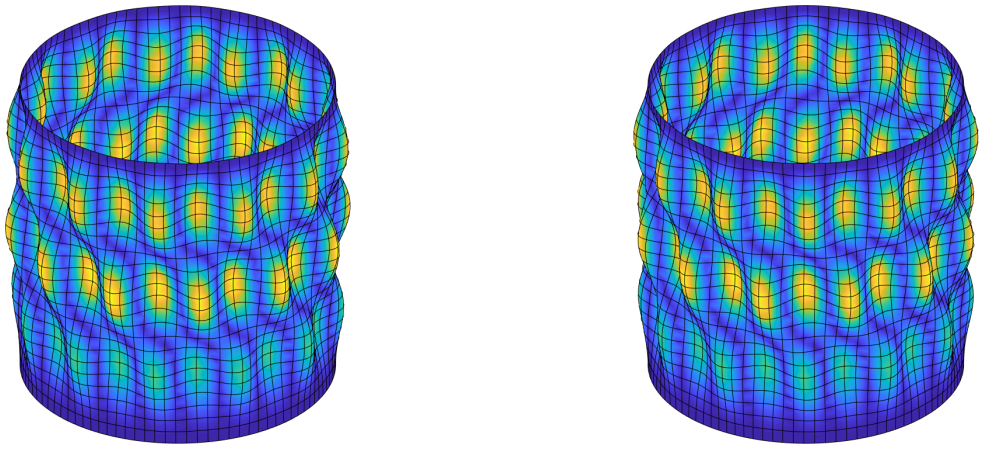
Figure 12: Laminate composite cylinder: model properties.

The cylinder is clamped at the bottom face and only the axial translation is allowed at the top surface. A uniformly distributed load along the top rim is applied in axial direction. The lowest buckling loads of the perfect structure are reported in Table 10 and Table 11 for the C_1 and the C_2 interpolation respectively. The corresponding buckling modes are depicted in Fig.13. Due to problem symmetries they occur in couples. Also for this test, C_1-$\bar{S}_0^2$, C_2-$\bar{S}_1^3$ and C_2-S_1^4 turn out to be particularly accurate and provide good results with a relatively coarse mesh in comparison with those usually employed in the FE literature [55].

In evaluating the initial post-buckling behavior a load imperfection is introduced by a concentrated force halfway up the cylinder axis. By including just one mode in the ROM, a good prediction of the limit load is obtained as shown in Fig.14 and confirmed by the comparison with the reference solution obtained using a very fine mesh and a full nonlinear analysis.

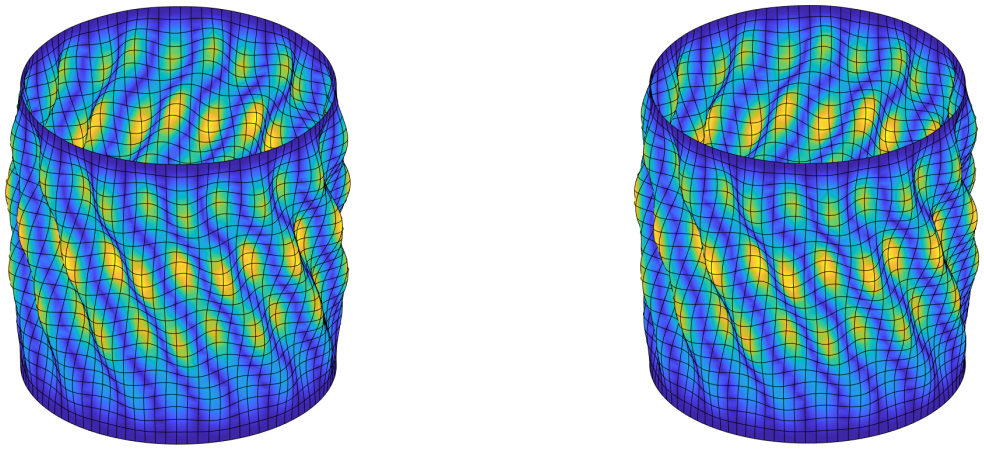
12 elm.			24 elm.			48 elm.		
$\bar{S}_1^3$	S_1^4	S_1^6	$\bar{S}_1^3$	S_1^4	S_1^6	$\bar{S}_1^3$	S_1^4	S_1^6
1.156	1.120	1.245	1.003	1.011	1.007	1.000	1.001	1.000
1.176	1.127	1.245	1.003	1.011	1.007	1.000	1.001	1.000
1.175	1.150	1.266	1.002	1.012	1.006	1.000	1.001	1.000
1.183	1.150	1.278	1.002	1.012	1.006	1.000	1.001	1.000

Table 11: Laminate composite cylinder: first 4 normalized buckling loads with C_2 interpolation.



(a) mode 1

(c) mode 2



(b) mode 3

(d) mode 4

Figure 13: Laminate composite cylinder: first 4 buckling modes.

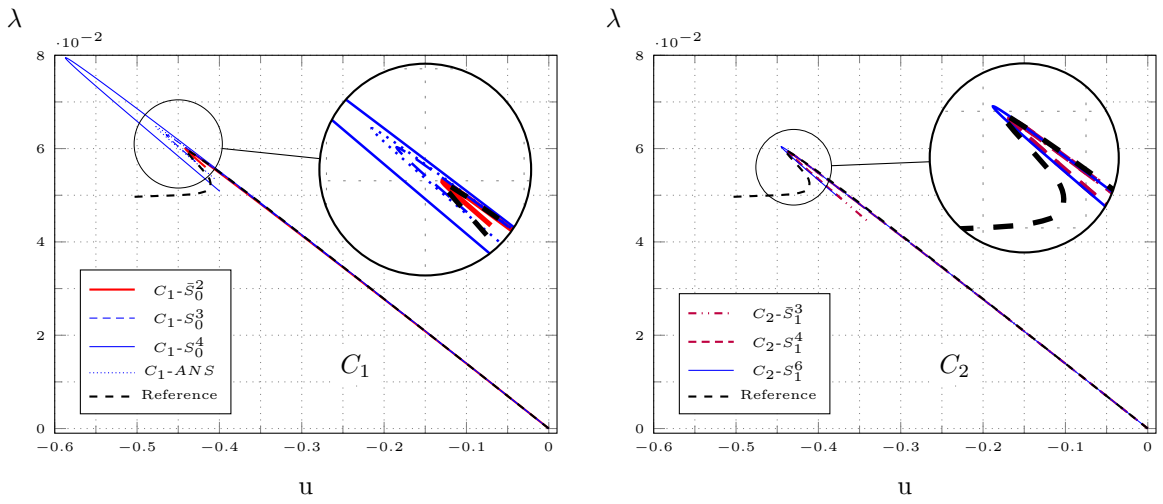


Figure 14: Laminate composite cylinder: equilibrium path using a 24×96 mesh

5. Summary and conclusions

The failure of slender composite shell structure is often dominated by buckling, while the material behavior is purely elastic. In this context, the Koiter method, which is a numerical formulation of Koiter's theory of elastic stability, represents a reliable and efficient tool of analysis. While standard path-following analyses solve the nonlinear equations of the discretized structure using all the discrete DOFs, the Koiter method uses a discretization technique just for the construction of a reduced model based on the first buckling modes, the corresponding corrective modes and the associated strain energy variations. Only the reduced nonlinear equations in a few unknowns, that is the modal amplitudes and the load factor, are then solved in order to obtain the equilibrium path.

In this work, we explored the use of IGA for the evaluation of the reduced model ingredients. The continuum shell problem was formulated in a Total Lagrangian way following the solid-shell concept, which makes it possible to avoid the use of finite rotations employing a simple Green Lagrange strain measure. The same interpolation was used for the geometry and displacement field. In particular, NURBS functions were employed for the middle surface quantities, obtained by refining those provided directly by a CAD model. Apart from the exact geometry, these highly continuous functions seem very suitable in approximating the deformed configuration of buckling problems. To maintain a low number of DOFs, a linear interpolation was adopted through the thickness of the shells. A modified generalized constitutive matrix was defined to prevent thickness locking and to make it easy to consider multi-layered composites. Path-wise reduced integrations were investigated to handle interpolation locking and to reduce the number of integration points. The mixed integration point strategy was used to re-write the displacement-based model into a mixed (stress-displacement) one, which has been shown to be more accurate and efficient in Koiter analyses. In particular, this approach makes it possible to avoid the evaluation of the fourth order strain energy variations, usually required to build the reduced order model.

The proposed numerical framework was tested in the analysis of common thin-walled composite structures under compression: plates, curved panels and cylinders. The results showed that the isogeometric model is able to furnish an excellent approximation of the buckling loads, the limit loads and the initial post-buckling behavior employing a very low number of DOFs coupled with the reduced number of integration points, which further increases the efficiency of the analysis. In particular the C_1-$\bar{S}_0^2$ and C_2-$\bar{S}_1^3$ approaches proves to be convenient because it requires just one integration point per element without spurious modes.

The resulting numerical tool is an efficient approach for the design of slender composite shells. Future developments will investigate its use in the optimization process of the layup.

Acknowledgment

The research leading to these results has received national funding from MIUR-PRIN project: "*Advanced mechanical modeling of new materials and structures for the solution of 2020 Horizon challenges*".

References

References

[1] G. Garcea, F. Liguori, L. Leonetti, D. Magisano, A. Madeo, Accurate and efficient a posteriori account of geometrical imperfections in Koiter finite element analysis, International Journal for Numerical Methods in Engineering-doi:10.1002/nme.5550.

[2] E. Barbero, A. Madeo, G. Zagari, R. Zinno, G. Zucco, Imperfection sensitivity analysis of laminated folded plates, Thin-Walled Structures 90 (2015) 128 – 139. doi:http://dx.doi.org/10.1016/j.tws.2015.01.017.

[3] V. Papadopoulos, G. Soimiris, M. Papadrakakis, Buckling analysis of I-section portal frames with stochastic imperfections, Engineering Structures 47 (SI) (2013) 54–66. doi:10.1016/j.engstruct.2012.09.009.

[4] E. Lindgaard, E. Lund, K. Rasmussen, Nonlinear buckling optimization of composite structures considering "worst" shape imperfections, International Journal of Solids and Structures 47 (22–23) (2010) 3186 – 3202. doi:http://dx.doi.org/10.1016/j.ijsolstr.2010.07.020.

[5] S. White, P. Weaver, Towards imperfection insensitive buckling response of shell structures-shells with plate-like post-buckled responses, Aeronautical Journal 120 (1224) (2016) 233–253. doi:10.1017/aer.2015.14.

[6] S. Henrichsen, P. Weaver, E. Lindgaard, E. Lund, Post-buckling optimization of composite structures using Koiter's method, International Journal for Numerical Methods in Engineeringdoi:10.1002/nme.5239.
[7] F. S. Liguori, A. Madeo, D. Magisano, L. Leonetti, G. Garcea, Post-buckling optimisation strategy of imperfection sensitive composite shells using Koiter method and Monte Carlo simulation, Composite Structures-doi:https://doi.org/10.1016/j.compstruct.2018.03.023.
URL http://www.sciencedirect.com/science/article/pii/S0263822317339776
[8] T. Rahman, E. Jansen, Finite element based coupled mode initial post-buckling analysis of a composite cylindrical shell, Thin-Walled Structures 48 (1) (2010) 25–32. doi:10.1016/j.tws.2009.08.003.
[9] E. Barbero, L. Godoy, I. Raftoyiannis, Finite elements for three-mode interaction in buckling analysis, International Journal for Numerical Methods in Engineering 39 (3) (1996) 469–488.
[10] E. Boutyour, H. Zahrouni, M. Potier-Ferry, M. Boudi, Asymptotic-numerical method for buckling analysis of shell structures with large rotations, Journal of Computational and Applied Mathematics 168 (1-2) (2004) 77–85. doi:10.1016/j.cam.2003.05.010.
[11] N. Silvestre, D. Camotim, Asymptotic-numerical method to analyze the postbuckling behavior, imperfection-sensitivity, and mode interaction in frames, Journal of Engineering Mechanics 131 (6) (2005) 617–632. doi:10.1061/(ASCE)0733-9399(2005)131:6(617).
[12] B. Schafer, L. Graham-Brady, Stochastic post-buckling of frames using Koiter's method, International Journal of Structural Stability and Dynamics 6 (3) (2006) 333–358. doi:10.1142/S0219455406001976.
[13] H. Chen, L. Virgin, Finite element analysis of post-buckling dynamics in plates-Part I: An asymptotic approach, International Journal of Solids and Structures 43 (13) (2006) 3983–4007. doi:10.1016/j.ijsolstr.2005.04.036.
[14] N. L. Rizzi, V. Varano, S. Gabriele, Initial postbuckling behavior of thin-walled frames under mode interaction, Thin-Walled Structures 68 (2013) 124 – 134. doi:http://dx.doi.org/10.1016/j.tws.2013.03.004.
[15] D. Magisano, L. Leonetti, G. Garcea, Koiter asymptotic analysis of multilayered composite structures using mixed solid-shell finite elements, Composite Structures 154 (2016) 296–308. doi:10.1016/j.compstruct.2016.07.046.
[16] D. Magisano, L. Leonetti, G. Garcea, Advantages of the mixed format in geometrically nonlinear analysis of beams and shells using solid finite elements, International Journal for Numerical Methods in Engineering 109 (9) (2017) 1237–1262. doi:10.1002/nme.5322.
[17] K. Liang, M. Ruess, M. Abdalla, The Koiter-Newton approach using von Karman kinematics for buckling analyses of imperfection sensitive structures, Computer Methods in Applied Mechanics and Engineering 279 (2014) 440–468. doi:10.1016/j.cma.2014.07.008.
[18] A. Madeo, R. Groh, G. Zucco, P. Weaver, G. Zagari, R. Zinno, Post-buckling analysis of variable-angle tow composite plates using Koiter's approach and the finite element method, Thin-Walled Structures 110 (2017) 1–13. doi:10.1016/j.tws.2016.10.012.
[19] E. Barbero, A. Madeo, G. Zagari, R. Zinno, G. Zucco, Koiter asymptotic analysis of folded laminated composite plates, Composites Part B: Engineering 61 (2014) 267–274. doi:10.1016/j.compositesb.2014.01.045.
[20] T. Rahman, S. Ijsselmuiden, M. Abdalla, E. Jansen, Postbuckling analysis of variable stiffness composite plates using a finite element-based perturbation method, International Journal of Structural Stability and Dynamics 11 (4) (2011) 735–753. doi:10.1142/S0219455411004324.
[21] W. Koiter, On the stability of elastic equilibrium, english transl. nasa tt-f10, 883 (1967) and affdl-tr70-25 (1970) Edition, Techische Hooge School at Delft, 1945.
[22] R. Casciaro, G. Salerno, A. Lanzo, Finite element asymptotic analysis of slender elastic structures: A simple approach, International Journal for Numerical Methods in Engineering 35 (7) (1992) 1397–1426. doi:10.1002/nme.1620350703.
[23] A. D. Lanzo, G. Garcea, R. Casciaro, Asymptotic post-buckling analysis of rectangular plates by HC finite elements, International Journal for Numerical Methods in Engineering 38 (14) (1995) 2325–2345.
[24] G. Garcea, Mixed formulation in Koiter analysis of thin-walled beams, Computer Methods in Applied Mechanics and Engineering 190 (26-27) (2001) 3369–3399.
[25] K. Sze, Three-dimensional continuum finite element models for plate/shell analysis, Prog. Struct. Engng. Mater 4 (2002) 400–407.
[26] S. Klinkel, F. Gruttmann, W. Wagner, A robust non-linear solid shell element based on a mixed variational formulation, Computer Methods in Applied Mechanics and Engineering 195 (1-3) (2006) 179–201. doi:10.1016/j.cma.2005.01.013.
[27] M. Schwarze, S. Reese, A reduced integration solid-shell finite element based on the eas and the ans concept—geometrically linear problems, International Journal for Numerical Methods in Engineering 80 (10) (2009) 1322–1355. doi:10.1002/nme.2653.
URL https://onlinelibrary.wiley.com/doi/abs/10.1002/nme.2653
[28] L. Vu-Quoc, X. G. Tan, Optimal solid shells for non-linear analyses of multilayer composites. I Statics, Computer Methods in Applied Mechanics and Engineering 192 (9-10) (2003) 975–1016. doi:10.1016/S0045-7825(02)00435-8.
[29] Q. Li, Y. Liu, Z. Zhang, W. Zhong, A new reduced integration solid-shell element based on EAS and ANS with hourglass stabilization, International Journal for Numerical Methods in Engineering (2015) 1885–1891arXiv:1010.1724, doi:10.1002/nme.
[30] G. Garcea, A. Madeo, R. Casciaro, The implicit corotational method and its use in the derivation of nonlinear structural models for beams and plates, J. Mech. Mater. Struct. 7 (6) (2012) 509–539. doi:10.2140/jomms.2012.7.509.
[31] G. Garcea, A. Madeo, G. Zagari, R. Casciaro, Asymptotic post-buckling FEM analysis using corotational formulation, International Journal of Solids and Structures 46 (2) (2009) 377–397.
[32] K. Sze, S.-J. Zheng, S. Lo, A stabilized eighteen-node solid element for hyperelastic analysis of shells, Finite Elements in Analysis and Design 40 (3) (2004) 319–340. doi:10.1016/S0168-874X(03)00050-7.

[33] Y. B. J. Austin Cottrell, Thomas J. R Hughes, Isogeometric Analysis: Toward Integration of CAD and FEA, 2009. doi:978-0-470-74873-2.
[34] V. P. Nguyen, C. Anitescu, S. P. Bordas, T. Rabczuk, Isogeometric analysis: An overview and computer implementation aspects, Mathematics and Computers in Simulation 117 (2015) 89 – 116. doi:https://doi.org/10.1016/j.matcom.2015.05.008.
[35] K. A. Johannessen, Optimal quadrature for univariate and tensor product splines, Computer Methods in Applied Mechanics and Engineering 316 (2017) 84 – 99, special Issue on Isogeometric Analysis: Progress and Challenges. doi:http://doi.org/10.1016/j.cma.2016.04.030.
[36] C. Adam, T. Hughes, S. Bouabdallah, M. Zarroug, H. Maitournam, Selective and reduced numerical integrations for NURBS-based isogeometric analysis, Computer Methods in Applied Mechanics and Engineering 284 (2015) 732–761. doi:10.1016/j.cma.2014.11.001.
[37] G. Garcea, R. Gonçalves, A. Bilotta, D. Manta, R. Bebiano, L. Leonetti, D. Magisano, D. Camotim, Deformation modes of thin-walled members: A comparison between the method of generalized eigenvectors and generalized beam theory, Thin-Walled Structures 100 (2016) 192–212. doi:10.1016/j.tws.2015.11.013.
[38] G. Garcea, L. Leonetti, D. Magisano, R. Gonçalves, D. Camotim, Deformation modes for the post-critical analysis of thin-walled compressed members by a Koiter semi-analytic approach, International Journal of Solids and Structures 110-111 (2017) 367–384. doi:10.1016/j.ijsolstr.2016.09.010.
[39] J. Caseiro, R. Valente, A. Reali, J. Kiendl, F. Auricchio, R. Alves de Sousa, Assumed natural strain NURBS-based solid-shell element for the analysis of large deformation elasto-plastic thin-shell structures, Computer Methods in Applied Mechanics and Engineering 284 (2015) 861–880. doi:10.1016/j.cma.2014.10.037.
[40] R. Echter, B. Oesterle, M. Bischoff, A hierarchic family of isogeometric shell finite elements, Computer Methods in Applied Mechanics and Engineering 254 (2013) 170–180. doi:10.1016/j.cma.2012.10.018.
[41] R. Bouclier, T. Elguedj, A. Combescure, Efficient isogeometric NURBS-based solid-shell elements: Mixed formulation and B-method, Computer Methods in Applied Mechanics and Engineering 267 (2013) 86–110. doi:10.1016/j.cma.2013.08.002.
[42] G. Garcea, G. Salerno, R. Casciaro, Extrapolation locking and its sanitization in Koiter's asymptotic analysis, Computer Methods in Applied Mechanics and Engineering 180 (1-2) (1999) 137–167.
[43] K. Sze, W. Chan, T. Pian, An eight-node hybrid-stress solid-shell element for geometric non-linear analysis of elastic shells, International Journal for Numerical Methods in Engineering 55 (7) (2002) 853–878. doi:10.1002/nme.535.
[44] D. Magisano, L. Leonetti, G. Garcea, How to improve efficiency and robustness of the Newton method in geometrically non-linear structural problem discretized via displacement-based finite elements, Computer Methods in Applied Mechanics and Engineering 313 (2017) 986 – 1005. doi:http://dx.doi.org/10.1016/j.cma.2016.10.023.
[45] S. Hosseini, J. J. C. Remmers, C. V. Verhoosel, R. de Borst, An isogeometric solid-like shell element for nonlinear analysis, International Journal for Numerical Methods in Engineering 95 (3) (2013) 238–256. doi:10.1002/nme.4505.
URL http://dx.doi.org/10.1002/nme.4505
[46] S. Klinkel, F. Gruttmann, W. Wagner, Continuum based three-dimensional shell element for laminated structures, Computers and Structures 71 (1) (1999) 43–62. doi:10.1016/S0045-7949(98)00222-3.
[47] M. Schwarze, S. Reese, A reduced integration solid-shell finite element based on EAS and the ANS concept: Large deformation problems, International Journal for Numerical Methods in Engineering 85 (3) (2011) 289–329. doi:10.1002/nme.
[48] J. F. Caseiro, R. A. F. Valente, A. Reali, J. Kiendl, F. Auricchio, R. J. Alves de Sousa, On the Assumed Natural Strain method to alleviate locking in solid-shell NURBS-based finite elements, Computational Mechanics 53 (6) (2014) 1341–1353. doi:10.1007/s00466-014-0978-4.
[49] L. Leonetti, F. Liguori, D. Magisano, G. Garcea, An efficient isogeometric solid-shell formulation for geometrically nonlinear analysis of elastic shells, Computer Methods in Applied Mechanics and Engineering 331 (2018) 159–183. doi:10.1016/j.cma.2017.11.025.
[50] W. T. Les Piegl, The NURBS book, 1997. doi:10.1007/978-3-642-59223-2.
[51] R. Bouclier, T. Elguedj, A. Combescure, Efficient isogeometric nurbs-based solid-shell elements: Mixed formulation and -method, Computer Methods in Applied Mechanics and Engineering 267 (2013) 86 – 110. doi:https://doi.org/10.1016/j.cma.2013.08.002.
[52] R. Echter, B. Oesterle, M. Bischoff, A hierarchic family of isogeometric shell finite elements, Computer Methods in Applied Mechanics and Engineering 254 (2013) 170–180. doi:10.1016/j.cma.2012.10.018.
[53] F. Maurin, F. Greco, W. Desmet, Isogeometric analysis for nonlinear planar pantographic lattice: discrete and continuum models, Continuum Mechanics and Thermodynamicsdoi:10.1007/s00161-018-0641-y.
URL https://doi.org/10.1007/s00161-018-0641-y
[54] S. G. Castro, R. Zimmermann, M. A. Arbelo, R. Degenhardt, Exploring the constancy of the global buckling load after a critical geometric imperfection level in thin-walled cylindrical shells for less conservative knock-down factors, Thin-Walled Structures 72 (2013) 76 – 87. doi:http://dx.doi.org/10.1016/j.tws.2013.06.016.
[55] D. Magisano, K. Liang, G. Garcea, L. Leonetti, M. Ruess, An efficient mixed variational reduced-order model formulation for nonlinear analyses of elastic shells, International Journal for Numerical Methods in Engineering 113 (4) (2018) 634–655. arXiv:https://onlinelibrary.wiley.com/doi/pdf/10.1002/nme.5629, doi:10.1002/nme.5629.
URL https://onlinelibrary.wiley.com/doi/abs/10.1002/nme.5629